OFF-FAULT DAMAGE ASSOCIATED WITH A LOCALIZED BEND IN THE NORTH BRANCH SAN GABRIEL FAULT, CALIFORNIA

A Thesis

by

ANDREW WILLIAM BECKER

Submitted to the Office of Graduate Studies of
Texas A&M University
in partial fulfillment of the requirements for the degree of

MASTER OF SCIENCE

Approved by:

Co-Chairs of Committee,	Judith S. Chester
	Frederick M. Chester
Committee Members,	Sorin Popescu
Head of Department,	Rick Giardino

December 2012

Major Subject: Geology

ABSTRACT

Structures within very large displacement, mature fault zones, such as the North Branch San Gabriel Fault (NBSGF), are the product of a complex combination of processes. Off-fault damage within a damage zone and first-order geometric asperities, such as bends and steps, are thought to affect earthquake rupture propagation and energy radiation, but the effects are not completely understood. We hypothesize that the rate of accumulation of new damage decreases as fault maturity increases, and damage magnitude saturates in very large displacement faults. Nonetheless, geometric irregularities in the fault surface may modify damage zone characteristics. Accordingly, we seek to investigate the orientation, kinematics, and density of features at a range of scales within the damage zone adjacent to an abrupt 13° bend over 425 m in the NBSGF in order to constrain the relative role of the initiation of new damage versus the reactivation of preexisting damage adjacent to a bend.

Field investigation and microstructural study focused on structural domains before, within, and after the fault bend on both sides of the fault. Subsidiary fault fabrics are similar in all domains outside the bend, which suggests a steady state fracture density and orientation distribution is established on the straight segments before and after the bend. The density of fractures within and outside the bend is similar; however, subsidiary fault orientations and kinematics are different within the bend relative to the straight segments. These observations are best explained by relatively low rates of damage generation relative to rates of fault reactivation during the later stages of faulting

on the NBSGF, and that damage zone kinematics is reset as the host rock moves into the bend and again upon exiting the bend. Consequently, significant energy released during earthquake unloading can be dissipated by reactivation and slip on existing fractures in the damage zone, particularly adjacent to mesoscale faults. Thus, areas of heightened reactivation of damage, such as adjacent to geometric irregularities in the fault surface, could affect earthquake rupture dynamics.

DEDICATION

To my loving parents, who have been a constant

source of encouragement and support

ACKNOWLEDGEMENTS

I would like to thank my committee co-chairs, Dr. Judith Chester and Dr. Frederick Chester, for giving me a chance as their student and patiently guiding me through the process. Also, I would like to thank my outside committee member, Dr. Sorin Popescu.

Thanks also to Alph Wright for being my dedicated field assistant. I would also like to thank Dr. Kenneth Hudnut for sharing his resources and expertise. I also want to extend my gratitude to the Southern California Earthquake Center and the National Science Foundation for providing the funds for my field research.

Finally, I want to especially thank my mother and father for their encouragement, and my brother for patiently listening to me rant about geology.

NOMENCLATURE

NBSGF	North Branch of the San Gabriel Fault
SGF	San Gabriel Fault
SBSGF	South Branch of the San Gabriel Fault
DEM	Digital Elevation Model
NDVI	Normalized Difference Vegetation Index
LIFD	Linear Intragranular Fracture Density
LSFD	Linear Subsidiary Fault Density
LTFD	Linear Transgranular Fracture Density
TFO	Transgranular Fracture Orientation

TABLE OF CONTENTS

LIST OF FIGURES

LIST OF TABLES

1. INTRODUCTION

Linear segments of faults typically are characterized by zones of localized slip, reflecting relatively high shear strain, that are surrounded by a zone of fractured rock [Figure 1, e.g., *Wallace & Morris,* 1986; *Chester et al.,* 1993; *Chester and Chester,* 1998]. The origin of the damaged zone primarily reflects 1) generation of damage in the breakdown or process zone of the rupture tip during propagation, and 2) generation of damage in rock as it moves past geometric irregularities in the main fault surface. Off-fault damage generated along a fault directly influences the energetics of a rupture by reducing the energy available for seismic wave radiation and fault slip acceleration [e.g., *Andrews,* 2005; *Chester et al.,* 2005; *Templeton and Rice,* 2008; *Biegel et al.,* 2008; *Sammis et al.,* 2009]. First order geometric asperities in the fault surface, such as bends and steps, can cause additional complexity in the spatial and temporal variations in stress along a fault, and therefore also can affect the rate of propagation of a rupture, and ultimately limit the extent of the rupture [e.g., *Segall and Pollard,* 1980; *King and Nabelek,* 1985; *Wesnousky,* 1988, 2006*; Harris and Day,* 1999; *Duan and Day,* 2008]. Variations in shear and normal prestress conditions local to the asperity, enhanced generation of off-fault damage, and reactivation of preexisting fractures at geometric irregularities all can lead to a decrease in propagation rates. The relative contribution of these processes is unclear. Critical to understanding rupture propagation and arrest during movement on mature faults is understanding the importance of new fracture

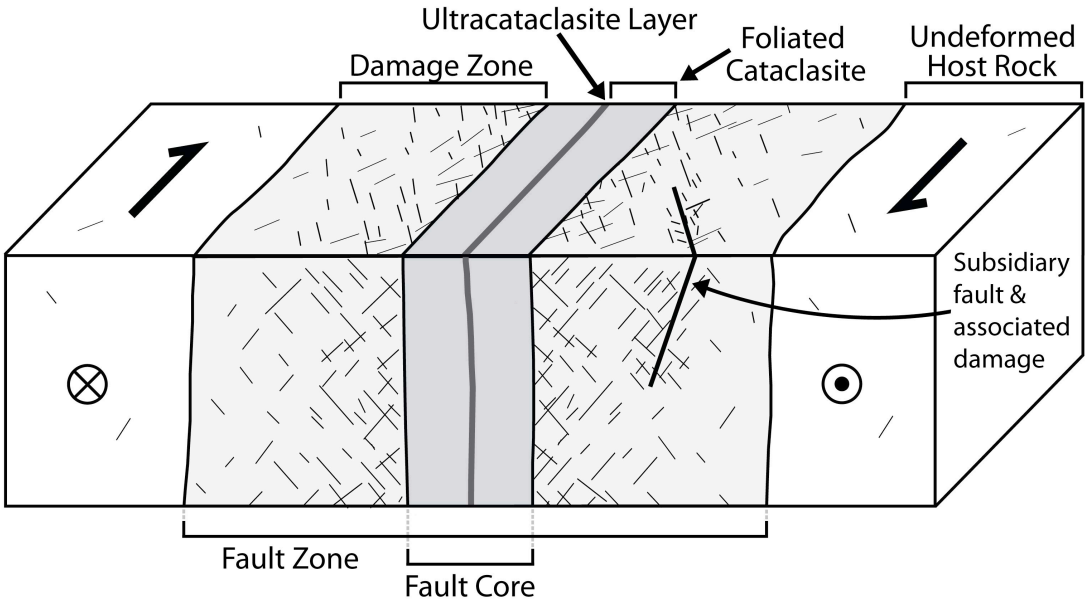

Figure 1. Characteristic fault zone model. Schematic diagram of a fault zone containing a single fault core along a linear segment of a large displacement strike-slip fault. Modified from *Mitchell and Faulkner* [2009] and *Chester et al.* [1993].

events relative to reactivated motion on and growth of existing fractures [e.g., *Andrews,* 2005; *Chester et al.,* 2005].

The density and distribution of deformation features in the damage zone of a mature fault reflect the cumulative response of this zone to fault-slip over the life of the fault [e.g., *Wilson et al.,* 2003]. A number of previous studies conclude that the rate of the damage accumulation is not constant, but instead starts high and decreases with increasing fault displacement [*Chester and Chester,* 1998; *Vermilye and Scholz,* 1998; *Sagy and Brodsky,* 2009]. Accordingly, I hypothesize that the rate of accumulation of new damage decreases as fault maturity increases, and damage magnitude saturates in very large displacement, mature faults, such as the North Branch San Gabriel Fault (16-20 km total displacement). If correct, this hypothesis suggests that as rock is translated past geometric irregularities in a mature fault surface, slip on the main fault surface may largely be accommodated by reactivated motion on preexisting fractures in the damage zone of the fault, and to a lesser extent by new fracture formation. As a result, the off-fault fracture fabric and density before, within, and after the geometric irregularity will mimic that found along straight segments of the main fault surface, but the kinematics of these features may vary with position. Subsidiary faults (shear fractures and small gouge zones) in the damage zone that are active only during slip on long, straight segments of the main fault will show a kinematic signature indicative of the average principal stress state of the main fault. In contrast, the kinematics of subsidiary faults that are reactivated when passing through a bend will reflect the perturbed local stress state created by the geometric irregularity.

The research objective of this proposal is to characterize the orientation and density distribution of fractures through the large bend in the San Gabriel Fault in the Transverse Ranges, California as a means to test two competing hypotheses: 1) most off-fault damage accumulates during displacement past geometric irregularities (i.e., at bends, jogs and step-overs) in fault surfaces, and 2) most off-fault damage accumulates early in a fault's displacement history, within the process zone, and therefore during the fault-tip propagation and fracture linkage stage, i.e., before the fault localizes to a continuous through-going macroscopic displacement surface. To test these hypotheses, I will characterize the variation in degree of damage in the off-fault region adjacent to the bend in a large displacement strike-slip fault.

1.1. Evolution of Off-fault Damage

The damage zone along a mature, large displacement fault is the product of different deformation processes occurring at a range of scales throughout the entire history of the fault [e.g., *Wilson et al.,* 2003]. In the initial stages of fault formation, according to the Anderson theory of faulting, tensile microfractures form perpendicular to the minimum principal compressive stress direction (Figure 2a), assuming a homogeneous stress state [*Anderson,* 1942]. With increased far-field stress, the microfractures may begin to coalesce as shear fractures begin to form at their tips, eventually forming through-going faults oriented at ~30˚ to the maximum principal compressive stress direction [Figure 2a, e.g., *Lockner et al.,* 1991, 1992; Figure 2b, e.g., *Brace and Bombolakis,* 1963; *Segall and Pollard,* 1983]. As the newly formed fault nucleates, a predictable distribution of damage forms at the propagating fault tip [Figure

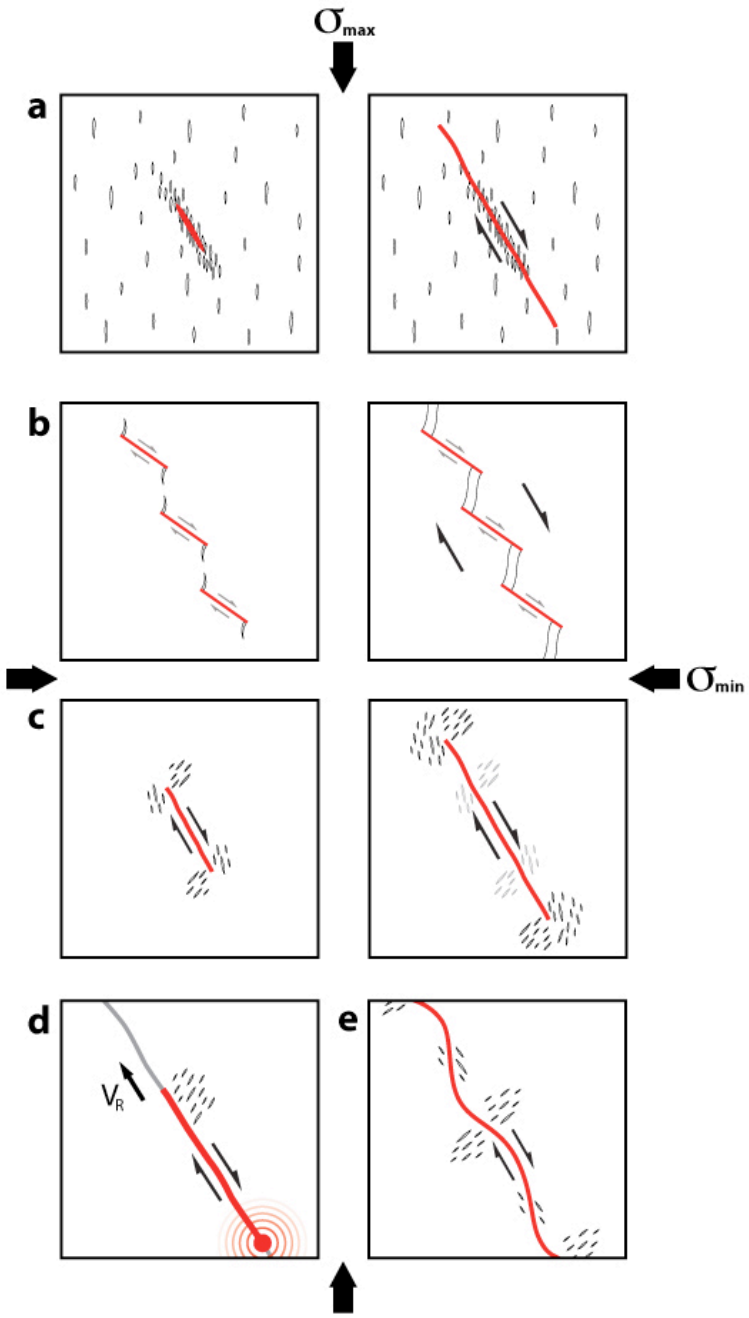

Figure 2. Damage accumulation models. Schematic diagrams illustrating models for damage accumulation during different stages of fault zone evolution. Modified from *Wilson et al.* [2005], *Blenkinsop* [2008], and *Mitchell and Faulkner* [2009]. (a) Assuming homogeneous stress, Anderson's model of fracture formation and subsequent fault formation. (b) Interaction between fault tip extension fractures along an en echelon geometry fault array and the subsequent linking. (c) Model for fault tip growth and the resulting fracture distribution due to stress concentrations at the tip. (d) Orientation of damage surrounding a propagating earthquake rupture tip, with V_R equal to the rupture velocity controlling the magnitude of fracture formation. (e) Fault model for fracture orientations along a wavy, frictional fault surface.

2c, e.g., *Cowie and Scholz,* 1992; *Scholz et al.,* 1993; *Vermilye and Scholz,* 1998]. A very specific stress state exists at the fault tip that depends on the location and sense-of shear [Figure 2c]. Subsequent earthquake ruptures are thought to produce similar damage distributions, but with a reduced magnitude, adjacent to each propagating rupture tip [*Cowie and Scholz,* 1992]. Variations in the magnitude of damage are dependent on a number of parameters, including the velocity of the earthquake rupture [Figure 2d; *Rice et al.,* 2005]. Furthermore, both field and modeling studies have suggested that damage also is produced behind the rupture tip as the damage zone experiences stress cycling and wear during movement along the irregular fault surface [Figure 2e, e.g., *Saucier et al.,* 1992; *Flinn,* 1977; *Chester and Logan,* 1986; *Chester and Fletcher,* 1997; *Chester and Chester,* 2000].

There are a number of additional factors that can affect the magnitude and orientation distribution of off-fault damage along faults, including 1) heterogeneous displacement magnitudes along the fault due to the location of numerous single rupture events on the three-dimensional fault surface, 2) variations in mechanical properties along and across the fault associated with the differences in lithology, 3) juxtaposition of more or less deformed fault slivers with different deformation histories, 4) spatial and temporal differences in pre-stress conditions, and 5) geometric irregularities in the fault surface such as bends (jogs) and discontinuous steps. Each of these factors must be considered in order to make a complete characterization of the off-fault damage uniquely attributed to a specific study area, such as the damage zone adjacent to a fault bend. The observed orientation and density distributions of fractures along the North Branch San

Gabriel Fault (NBSGF) will be analyzed in light of these conceptual and mechanical models in order to determine which processes are primarily responsible for the accumulation of off-fault damage along straight segments and in the curved region of the fault.

1.2. Role of Off-fault Damage to Earthquake Energetics

Previous models have linked the macroscopic energy budget to physical processes within a fault zone during dynamic earthquake rupture [e.g., *Kanamori and Heaton,* 2000; *Kanamori,* 1994]. Current models hold that elastic strain energy released during an earthquake is partitioned between the fracture energy, frictional heat, and the energy radiated as seismic waves [e.g., *Chester et al.,* 2005; *Kanamori and Heaton,* 2000; *Venkataraman and Kanamori,* 2004]. The preexisting damage that is present within a fault zone, and the processes that occur as the result of the passage of an earthquake rupture, influence how the elastic strain energy is partitioned [*Chester et al.,* 2005]. The formation and reactivation of off-fault damage in a fault zone also is known to directly influence rupture energetics by reducing the energy available for seismic wave radiation and acceleration of slip [e.g., *Andrews,* 2005; *Chester et al.,* 2005; *Templeton and Rice,* 2008; *Biegel et al.,* 2008; *Sammis et al.,* 2009]. At this time there are relatively few quantitative characterizations of damage along faults that can constrain energy partitioning during fault slip [e.g., *Chester et al.,* 2005; *Mitchell & Faulkner,* 2009]. Detailed descriptions and quantification of the density and orientation distribution of fracture damage before, within, and after a geometric irregularity in a fault surface

will increase our understanding of the origin and evolution of damage zones, and help constrain models of dynamic rupture propagation along irregular fault surfaces.

2. GEOLOGY OF THE NORTH BRANCH OF THE SAN GABRIEL FAULT AND SPECIFIC STUDY AREA

The North Branch of the San Gabriel Fault, located in the central Transverse Ranges of southern California, is likely one of the most deeply exhumed traces of the San Andreas system (Figure 3). The NBSGF is a large-displacement, right-lateral strike-slip segment of the San Gabriel Fault (SGF), which lies in the uplifted and dissected western San Gabriel Mountains [*Ehlig*, 1973, 1981]. At the macroscopic scale the fault forms a single, continuous trace that trends approximately east west in the region of Bear Creek. The NBSGF bends to the northwest just west of Devil's Canyon and the continues to intersect with the South Branch of the San Gabriel Fault (SBSGF) west of Big Tujunga Creek (Figure 3).

The juxtaposition of granodiorite and other igneous assemblages along the NBSGF, and the fabric of nearby subsidiary faults are consistent with approximately 16 to 21 km of cumulative right-lateral displacement [*Ehlig*, 1981; *Chester et al.*, 1993]. The NBSGF was active during the Miocene, approximately 12 to 5 million years ago, as the first onshore trace of the San Andreas Fault [*Crowell*, 1982b; *Powell*, 1993].

Exhumation of the San Gabriel Mountains, subsequent to displacement on the NBSGF, is constrained to about 3 km based on apatite fission-track and (U-Th)/He thermochronology, and estimates of relative denudation rates [*Blythe et al.*, 2000]. Exhumation magnitudes can be somewhat greater in the deeply incised canyons along the West Fork of the San Gabriel River. The majority of uplift forming the modern San

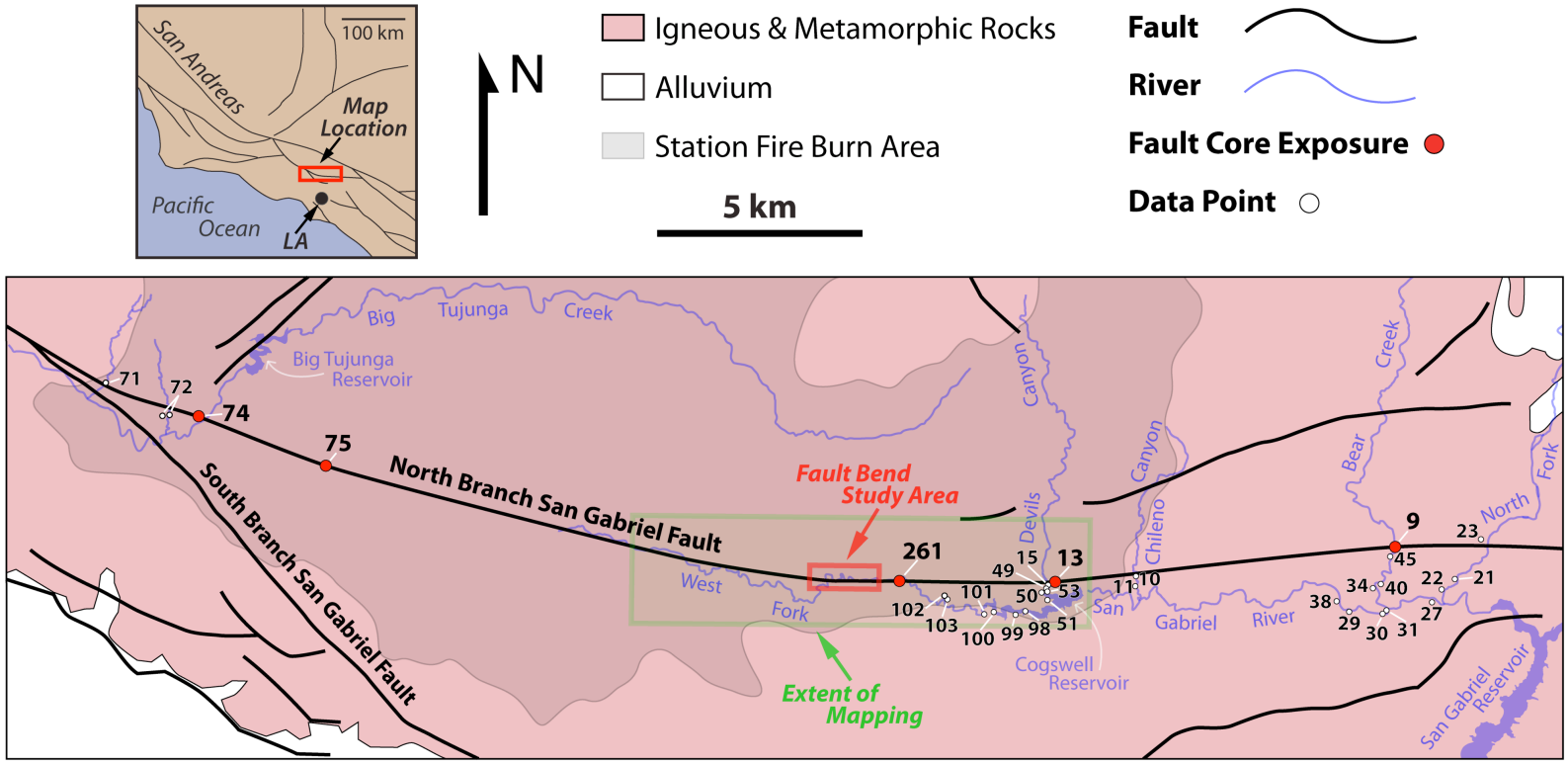

Figure 3. Geologic map of the San Gabriel Fault. The field area of interest relative to Los Angeles (L.A.), Big Tujunga Reservoir (west), and San Gabriel Reservoir (east). The location context map (upper left), location of the fault bend study area (in red) and the extent of mapping (in green), fault core exposures, measurement data points, and the extent of the Station Fire burn area are included. Modified from *Chester et al.* [2004].

Gabriel Mountains reflects displacement on the Sierra Madre-Cucamonga thrust system and additional exhumation associated with regional arching of the Transverse Ranges [e.g., *Oakeshott*, 1971; *Morton and Matti*, 1987; *Blythe et al.*, 2000].

The North Branch of the San Gabriel Fault exhibits a distinct structure marked by extreme localization of slip in a single fault core composed of a well-defined ultracataclasite layer, surrounded by a damage zone up to 100 m wide [Figures 1; e.g., *Anderson et al.*, 1983; *Chester et al.*, 1993; *Evans and Chester,* 1995]. Microscale features and particle size distributions in the damage zone indicate that cataclastic processes dominated during faulting [*Chester et al.*, 1993, 2004], which can be explained through a constrained comminution model devised by *Sammis et al.* [1987].

Strike-slip subsidiary faults cutting the damage zone of the NBSGF exhibit quasi-conjugate geometries [*Chester et al.*, 1993]. Using paleostress inversion techniques, *Chester et al.* [1993] determined that the maximum principal compressive stress compatible with these faults was oriented approximately 60° to 80° to the NBSGF. The meso- and microscale linear fracture density in the damage zone of the NBSGF displays some significant local variations, but overall show an increase in linear fracture density with decreasing distance to the ultracataclasite layer [*Chester et al.*, 2004]. The linear fracture density data also indicates an approximate fault zone width of 100 m from the ultracataclasite layer to the damage zone edge [*Chester et al.*, 2004].

Lithologic variations in the damage zone of the NBSGF can, in large measure, be attributed to previous igneous and metamorphic events [*Anderson et al.,* 1983]. The NBSGF damage zone lithology is varied at the local scale, along strike and with

perpendicular distance from the fault trace. Changes in lithology range from subtle mineralogy variations to the presence of exotic, relatively less deformed slivers of rock that were incorporated during displacement on the NBSGF. Varying degrees of foliations are seen within existing units and in already foliated units, such as the Mendenhall Gneiss. Zeolite-grade alteration (laumontite-chlorite) events also likely occurred prior to displacement on the NBSGF [*Anderson et al.*, 1983; *Evans and Chester*, 1995].

This study began with an initial reconnaissance focused on an approximately 14 km segment of the NBSGF that extended up to 1 km north and south of the fault, depending on the accessibility along north-south trending canyons (Figure 3). The study area extends about 1500 m along the fault trace, and up to 125 m to the north and south of the trace. About 30-40% of this latter region is accessible and outcrop sizes range from 100 sq m to 200 sq m, on average. Previous studies of the NBSGF were even more limited due to the rugged topography and extremely dense vegetation. The field area, however, recently experienced a significant reduction in vegetation and enhanced mass wasting because of the Station Fire (26 August to 16 October, 2009). The Station Fire provides a unique opportunity to study excellent exposures of the fault core within the North Branch San Gabriel Fault zone (Figure 3).

3. METHOD OF STUDY

3.1. Field Study

3.1.1. Field Preparations

In preparation for fieldwork, detailed topographic base maps were constructed using digital elevation models (DEM) produced from geographic synthetic aperture radar (GeoSAR) data. Quick Terrain Modeler® and Environment for Visualizing Images® (ENVI) were used to process the GeoSAR data and to create a DEM, which was then imported into ArcMap® to format the final base maps. The base maps span the length of the San Gabriel Fault in the San Gabriel Mountains at scales of 1:10,000, 1:5000, and 1:1000. The location of the NBSGF on the base maps was determined from published and unpublished geologic maps [*Chester et al.*, 1993; *Evans and Chester*, 1995; *F.M. Chester*, personal communication, 2010], topographic features evident in the GeoSAR DEM, and linear features identified by application of a Sobel filter to Landsat 5 Thematic Mapper (TM) multispectral images. The Normalized Difference Vegetation Index (NDVI) graphic indicator was also applied to Landsat 7 Enhanced Thematic Mapper Plus (ETM+) multispectral imagery to locate sparsely vegetated areas along the NBSGF.

The GeoSAR DEM was analyzed by rendering the three-dimensional topographic surface with a hillshade and increasing the vertical exaggeration to accentuate topographic features (Figure 4). Rendering with an increased vertical exaggeration has been used for a variety of applications in previous studies, and

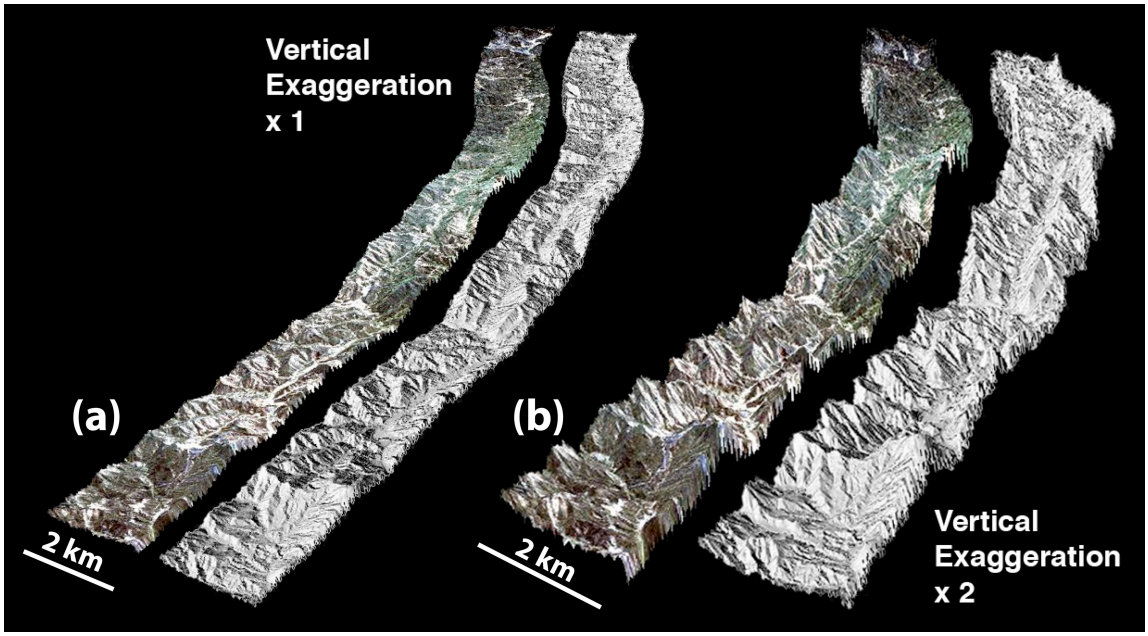

Figure 4. Vertical exaggeration applied to NBSGF trace. Both (a) and (b) have a pan-sharpened Landsat 7 ETM+ image applied to the GeoSAR DEM on the left and the hillshade applied to the DEM on the right. (a) Displays 1x vertical exaggeration, and (b) shows 2x vertical exaggeration.

facilitates the identification of the fault surface in the base maps [e.g., *Dekker et al.*, 1991; *Harris and Cooper*, 2002; *Luo and Stepinski*, 2008; *Wechsler*, 2009]. The Sobel filter method, which uses an edge detection algorithm to highlight linear features in particular orientations, was used to locate the fault surface in ENVI (Figure 5). Finally, in an effort to find the best areas for field study, the NDVI method was executed in ENVI to clearly distinguish the burned areas along the NBSGF from those that are densely vegetated (Figure 6).

3.1.2. Field Observations

Initial field reconnaissance was conducted to locate mesoscale exposures of the NBSGF, define macroscopic and mesoscopic structural domains, locate large well-preserved outcrops for data and sample collection, and field check the mesoscale geometry of the fault through the macroscopic bend (Figure 3).

The off-fault damage in all structural domains before, within, after, and on both the compressional (north) and extensional (south) sides of the bend in the NBSGF surface was quantified through study of outcrops and hand-size samples (Figure 7). Specific data that were collected within each structural domain include the distribution, type (i.e., shear versus joint), orientation, and length of meso- and macro-scale fractures. Detailed petrologic and microstructural data were collected from the samples.

3.1.2.1. Linear Fracture Density as a Function of Distance from the Main Fault Surface

The magnitude of mesoscale fracture damage (subsidiary faults, fractures, and veins), as a function of distance from the ultracataclasite of the fault core, was

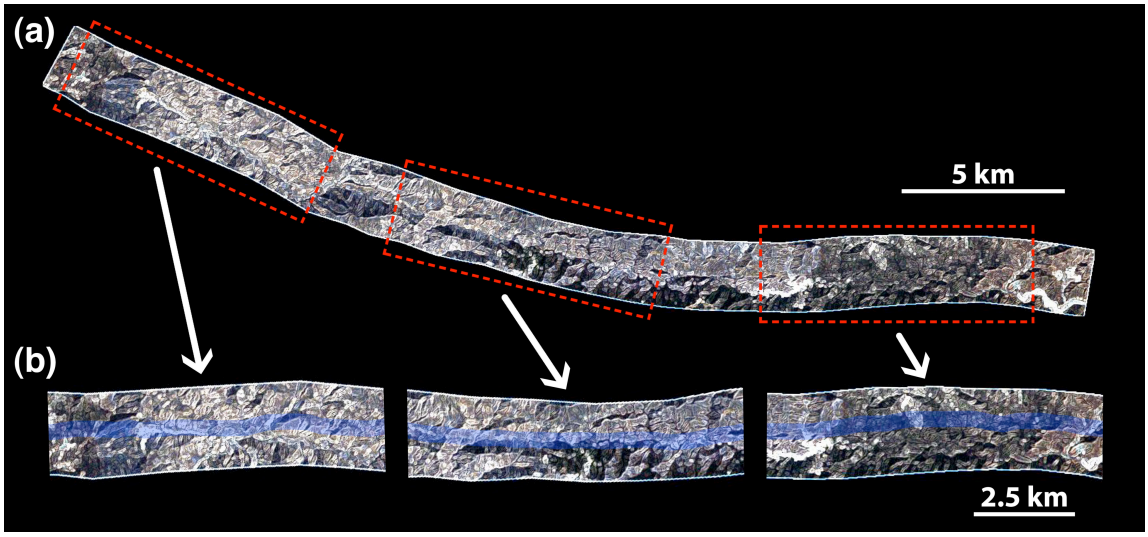

Figure 5. Sobel filter applied to NBSGF trace. (a) The Sobel filter applied to the Landsat 5 TM image, and (b) the magnified images with the fault zone highlighted in blue.

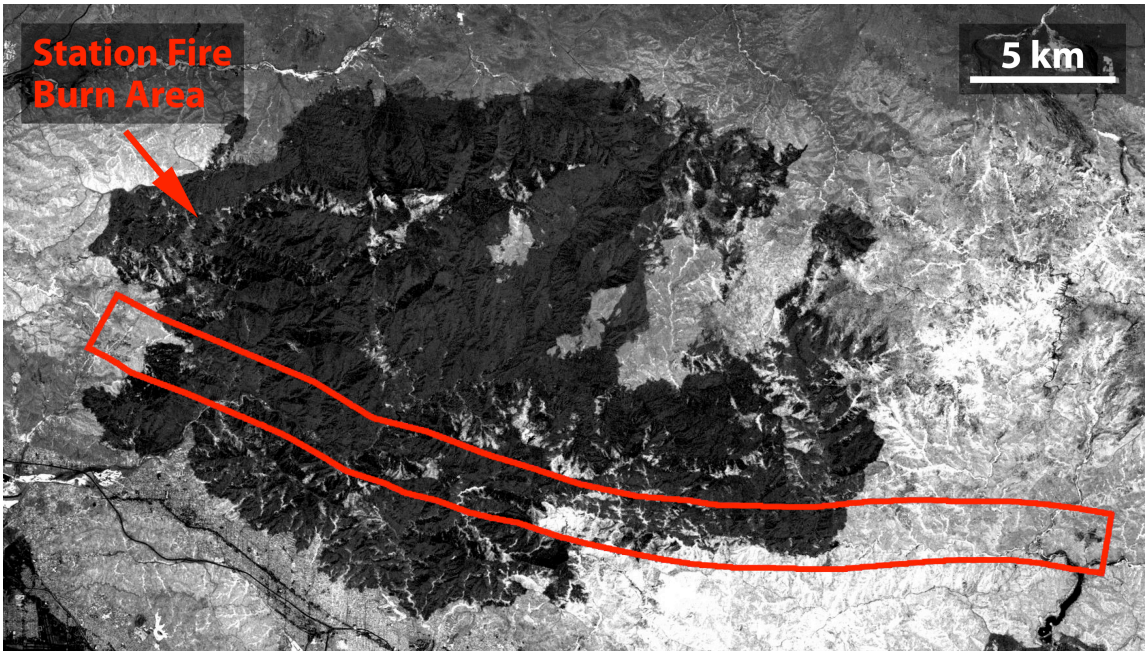

Figure 6. Vegetation index applied to NBSGF trace. Landsat 5 TM image (post-fire) with a vegetation index (NDVI) of the burn area and the fault trace swath highlighted in red.

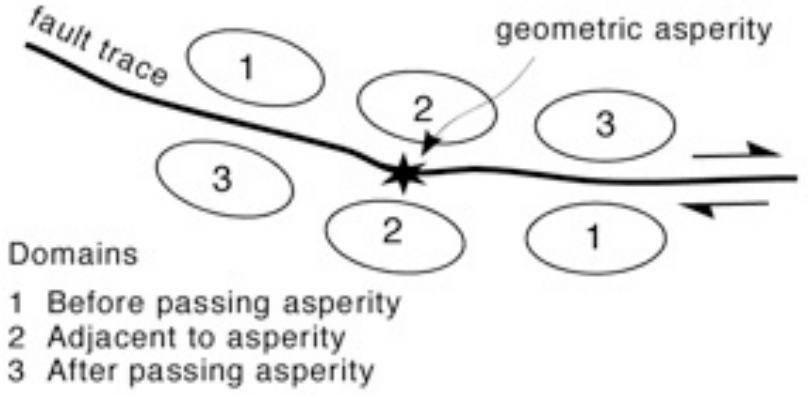

Figure 7. Fault bend structural domains. Schematic diagram showing domains before, adjacent to, and after the geometric asperity (fault bend). Illustrating the domains that might be impacted by the geometric asperity.

characterized using methods described by *Chester et al*. [1993] and *Neal* [2002]. This damage index was estimated along nine traverses that were perpendicular and one approximately parallel to the main fault surface. The traverses sample regions north and south of the fault, and each structural domain defined by the fault bend (Figure 7).

At each measurement station, the number of fractures crossing two randomly oriented, orthogonal count lines of equal length were recorded. The number of fracture intercepts along the count line, divided by the length of the count line, defines the linear fracture density at that station. Previous studies have consistently shown that the linear fracture density increases with decreasing proximity to the ultracataclasite [e.g., *Chester et al.*, 1993], to best capture the data the spacing between measurement stations was reduced systematically with decreasing distance to the fault. A total count line length of 0.61 m was used within meters of the main fault surface; at greater distances, the length of the count line was 1.83 m. The count line was spun an arbitrary amount at each measurement station to reduce an orientation bias during sampling.

3.1.2.2. Subsidiary Fault Orientation and Kinematic Data

Subsidiary fault orientation and kinematic data were collected in each structural domain. Data collected includes the average orientation of the fault plane and slip-lineations, sense-of-shear, presence and composition of gouge, and distance from the main fault surface. A sketch was drawn at each outcrop to illustrate cross-cutting relationships. Subsidiary fault data were collected from five larger outcrops with a size range up to 21 m by 11 m, and five smaller (1.8 m by 1.2 m) outcrops.

3.1.3. Sampling Techniques

Oriented samples were collected at key locations relative to the fault bend using standard sampling collection techniques [e.g., *Friedman,* 1969]. Samples were taken along or near the fracture density traverses and from subsidiary fault measurement stations (Table 1). Samples were chosen to represent the key lithologies present adjacent to the fault, and were collected at least one meter from large subsidiary faults to avoid the influence of local damage associated with movement along that fault.

3.2. Petrologic Descriptions

To help define the lithologic variation in the field area, a select set of thin sections were stained to distinguish potassium feldspar, plagioclase feldspar, and quartz. Each stained section was etched with hydrofluoric acid vapor, dipped in barium chloride solution, and treated with potassium rhodizonate to stain plagioclase feldspar red [*Bailey and Stevens*, 1960], and with cobaltinitrite to stain potassium feldspar yellow [e.g., *Gabriel and Cox*, 1929].

The volume percent of different mineral phases in each thin section was characterized by quantitative modal analysis following methods modified from *Anders and Wiltschko* [1994] and *Wilson et al.* [2003]. Point counts were made on a standard petrographic microscope with a mechanical stage. Mineral counts were made about every 1 mm along traverse lines spaced 1 mm apart, to sample up to 650 points per thin section. The general composition of each sample was determined by plotting the three main mineral phases on IUGS ternary igneous classification diagrams [e.g., *Le Bas and Streckeisen,* 1991].

Table 1.
Sample Location and Description

Sample	Distance from Fault (m)	Closest Mesoscale LFD Traverse		Domains**	Rock Type	Grain Size	Foliation Degree	Foliation Orientation***
		Traverse #	Distance to Sample (m)*					
227-9	4.8	3	0.9	Within (N)	Quartz Diorite	Coarse	-	-
231-3	5.4	10	0.3	Before (S)	Quartz Diorite	Medium	-	-
259-5	5.6	7	0.6	After (N)	Tonalite	Medium	weak	045°, 70°
231-2	7.2	10	0.0	Before (S)	Tonalite	Coarse	moderate	071°, 70°
230-17	9.0	6	1.0	After (N)	Tonalite	Medium	weak	119°, 77°
13-N[P]	10.1	-	-	Before (S)	Tonalite	Medium	-	-
227-11	10.7	2	1.0	Within (S)	Tonalite	Medium	weak	250°, 23°
13-Z[P]	15.9	-	-	After (N)	Tonalite	Fine	moderate	100°, 71°
230-11	17.8	5	0.8	Before (S)	Quartz Diorite	Medium	-	-
227-12	18.7	2	1.2	Within (S)	Tonalite	Medium	moderate	014°, 16°
230-19	19.6	6	0.6	After (N)	Calcite-Rich Tonalite	Very Fine	-	-
13-Beta[P]	48.4	-	-	After (N)	Tonalitic Gneiss	Medium	strong	308°, 70°
13-Phi[P]	69.2	-	-	Before (S)	Granodiorite	Medium	-	-

*Distance between the sample and the traverse, measured parallel to the NBSGF.

**Domains relative to the fault bend, either North (N) or South (S) of the San Gabriel Fault.

***Foliation orientations use the right-hand rule convention.

P - Samples collected during previous studies.

weak = < 20%; moderate = 20-40%; strong = > 40%

3.3. Microstructural Characterizations

For the microstructural characterization, one to three mutually perpendicular thin sections were made from key oriented samples (Table 1). These sections are defined by outward normals that parallel north, west, and the horizontal plane (Figure 8). Plane- and cross-polarized light digital image scans were taken of each thin section and used as location maps for the density and orientation measurements. Thin sections were used to collected thin section scale transgranular fracture density and orientation data, and grain scale intragranular fracture density data.

3.3.1. Intermediate Scale Fracture Density Measurements

Two linear fracture density estimates were acquired at the scale of a whole thin-section. The first estimate quantifies the number of transgranular fractures that intercept a 10 mm square grid, and the second is based on a 2.5 mm square grid. These measurements were made on the image scans and checked for accuracy on the petrographic microscope. The measurement procedure was similar to that described by *Anders and Wiltschko* [1994] and *Takagi et al.* [2012]. The number of fracture intercepts, length of each fracture, type of each fracture (i.e., open, sealed, cataclastic zone, gouge zone), and type of fracture fill (e.g., quartz, calcite) were noted. For the 10 mm grid, only fractures greater than 10 mm in length were recorded; for the 2.5 mm grid, fractures greater than 2.5 mm and less than 10 mm were recorded. A linear fracture density was determined for the grid lines parallel to the thin section's long dimension and averaged with that determined for the short dimension to give a linear fracture density for the whole thin section.

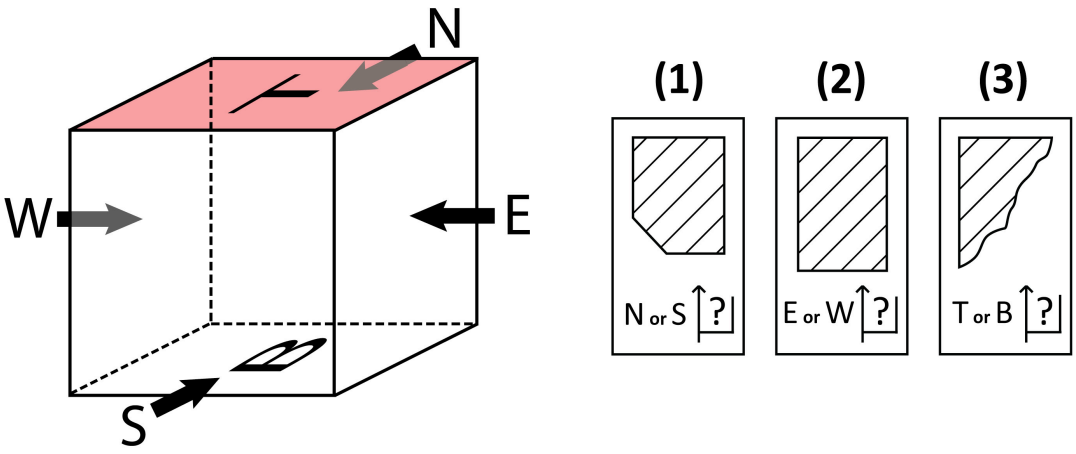

Figure 8. Oriented sample guide cube. Schematic diagram of the guide cube used to orient each sample. Three mutually perpendicular thin sections are cut from each sample: (1) north or south plane, (2) east or west plane, and (3) top or bottom plane.

3.3.2. Microscale Fracture Density Measurements

Linear intragranular fracture density (LIFD) data were collected with a mechanical stage on a petrographic microscope similar to *Anders and Wiltschko* [1994] and *Neal* [2002]. Quartz grains larger than 0.25 mm in diameter that fell on or adjacent to a 100-point square grid were analyzed. For quartz-poor samples, feldspar grains were substituted when necessary. Feldspars have two well-defined cleavage planes that intersect at 90˚. During brittle fracture these minerals may preferentially fracture along their cleavages. The cleavage orientations, therefore, may bias the fracture analysis that is directed at understanding the role of the fault bend in creating off-fault deformation. To assess if such a bias exists, feldspar grains were analyzed separately. In non-foliated samples, this bias should be small. In foliated samples, this bias may be significant. Data recorded in each grain includes the mineral phase, orientation of the count line, length of the count line, number of fractures that cross the count line, and type of fractures (i.e., open, sealed, or healed). The orientation of the count line was determined ahead of time by generating a list of random numbers from 0 to 360. This number defined the main count line orientation at each grid intersection. This count line was positioned within each grain such that it spanned the longest dimension of the grain in the specified orientation. The same method was used for the perpendicular count line, but only in the quartz grains to increase the sampling of quartz grains in these quartz-poor samples.

3.3.3. Transgranular Fracture Orientations

The orientation of transgranular fractures was determined using methods modified from *Laubach* [1988] and *Kulander et al.* [1979], using a mechanical stage on

a petrographic microscope, and from *Friedman* [1969] and *Wilson et al*. [2003], using a four-axis universal stage. The universal stage measurements were conducted on one to three mutually perpendicular thin sections per sample, and the flat-stage data were collected from just the horizontal plane sections. Each fracture measured was noted on the digital thin section scans. The orientation, thickness, type (i.e., open, sealed, cataclastic zone, gouge zone), type of fill, and all crosscutting relationships were noted for the fractures measured. For the universal stage measurements, care was taken to avoid sample bias as described in detail by *Wilson* [1999].

4. RESULTS

4.1. Field Observations

4.1.1. Field Reconnaissance Using Remote Sensing Techniques

Vertical exaggeration and the Sobel filter were used to locate geometric irregularities in the NBSGF surface highlighted by topography prior to field reconnaissance (Figures 4-5). Once in the field, however, it was difficult to field-check each of these geometric features at the resolution that they were initially identified because of limited outcrop size and the spacing between outcrops (Figures 9a and 9c). Conversely, the NDVI technique proved very useful in locating sparsely vegetated areas along the NBSGF (Figures 9b and 9d). The NDVI process of determining outcrop quality and accessibility ahead of time made the initial stage of field work much more successful.

4.1.2. Study Area Description

The study area highlights a large-scale bend that runs primarily along the San Gabriel River, about 3 km west of the Cogswell Reservoir (Figure 10). The samples were collected in each structural domain relative to the fault bend, at a range of distances from the fault surface, and from representative lithologies in the detailed study area. Samples were collected within 50 m to 1.6 km from the fault bend, with one sample from previous studies about 5.3 km west of the bend [Table 1; Figure 10a; *Chester and Chester*, unpublished data, 2010].

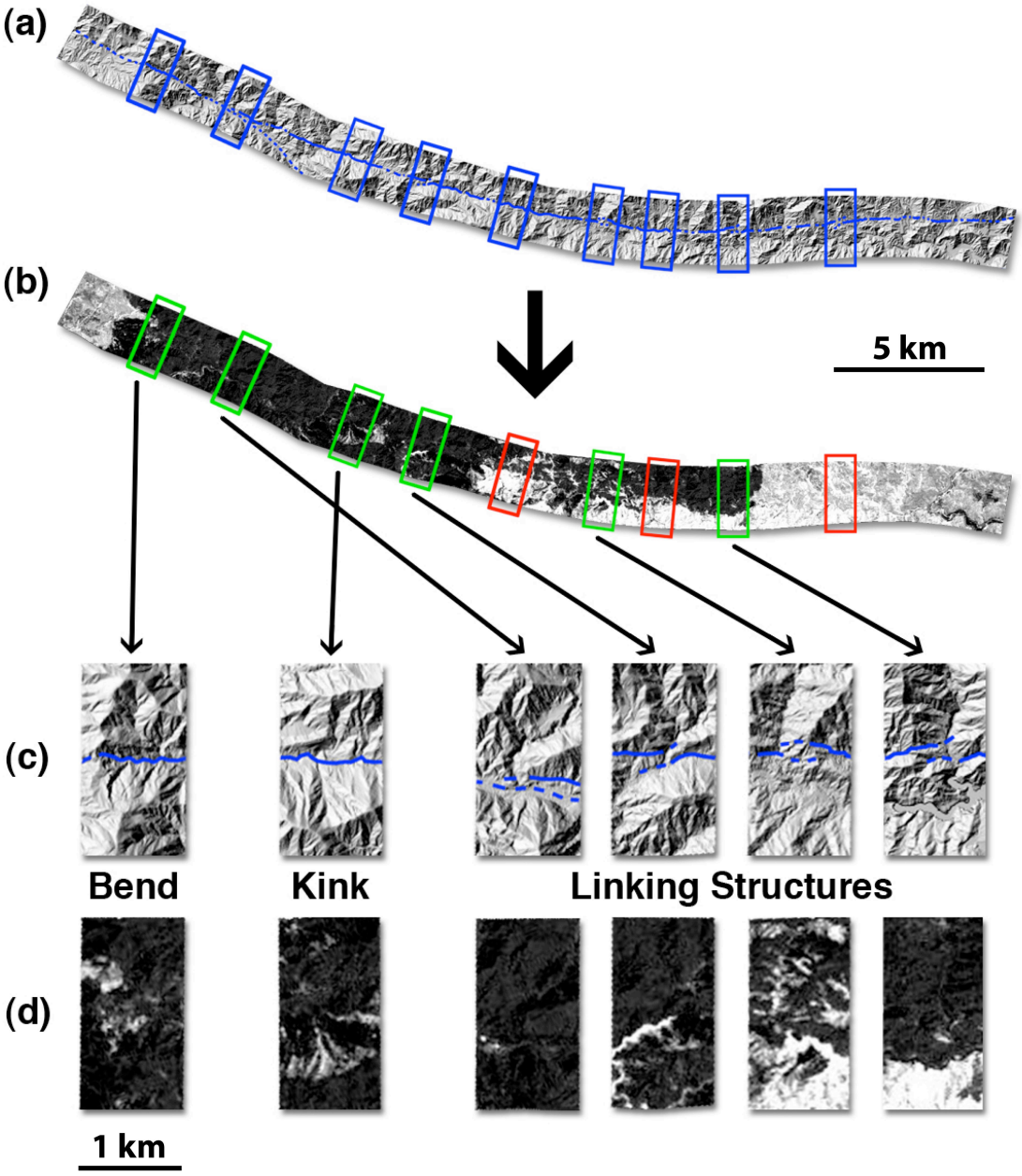

Figure 9. Field reconnaissance locations. The GeoSAR DEM hillshade (a) shows the full trace of the fault surface highlighted along with the areas of interest in blue. The NDVI image (b) shows the areas with acceptable vegetation levels in green and those still inaccessible in red. Both (c) and (d) together allow for a comparison of the fault irregularities with the vegetation levels in each location.

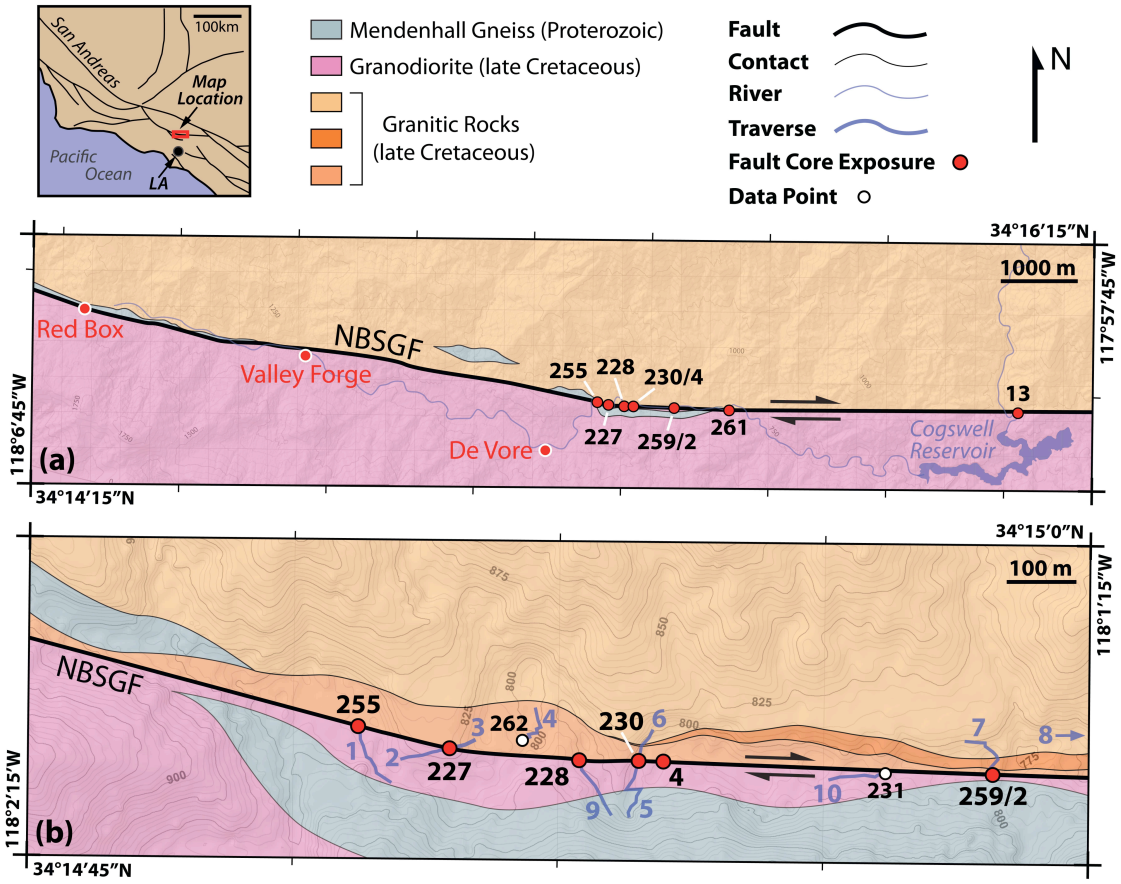

Figure 10. Geologic map of the NBSGF. The field area location along the NBSGF, located relative to Los Angeles (upper left). (a) Initial field area with geographic context relative to campsites and Cogswell Reservoir in the Angeles National Forest, and (b) the fault bend study area including fracture density traverses. Modified from *Chester et al.* [2004].

4.2. Petrologic Descriptions

The rock units described in this study are similar to those units defined by previous studies along the NBSGF [Table 1; *Anderson et al.,* 1983; *Chester et al.,* 1993; *Evans and Chester,* 1995]. South of the NBSGF, within the study area, the units include Cretaceous tonalites with some quartz diorites and granodiorites that are foliated to different degrees. The Proterozoic age Mendenhall Gneiss is also present south of the fault, and to the north as scattered slivers (Figure 10). The units north of the NBSGF are similar in composition to the southern units, but in detail the lithology varies reflecting the presence of lenses that have subtle differences in mineralogy with distance from the fault.

The samples collected along the NBSGF represent the variety of igneous plutonic rocks of the San Gabriel Basement Complex, and different degrees of foliation that is assumed to predate displacement of the NBSGF [Table 1; *Anderson et al*., 1983]. The samples are composed of mainly quartz and plagioclase feldspar, with some potassium feldspar, and trace amounts of calcite, chlorite, phyllosilicates, and other minerals (Table 2). The quartz grains display undulatory extinction. Plagioclase feldspar grains are altered to different degrees by sericitization. Potassium feldspar grains are relatively uncommon in most samples. Calcite, chlorite, and biotite are present as fill within multiple generations of fractures that occur in varying densities in the majority of the samples. The average grain size of the samples is mostly medium, with a few samples that reach coarse and fine to very fine grain sizes.

Table 2.
Petrology of San Gabriel Fault Samples

Sample	Distance from Fault (m)	Domains*	% Quartz	% Potassium Feldspar	% Plagioclase Feldspar	% Calcite	% Chlorite	% Other**
231-3	5.4	Before (S)	14.4	0.3	58.6	11.9	2.6	12.2
231-2	7.2	Before (S)	14.9	0.0	54.7	21.1	8.8	0.5
13-N	10.1	Before (S)	26.2	2.3	61.4	1.0	0.3	8.8
230-11	17.8	Before (S)	12.2	0.0	63.4	7.9	5.0	11.5
13-Phi	69.2	Before (S)	29.5	17.6	48.5	0.0	0.3	4.1
227-9	4.8	Within (N)	15.5	7.1	64.2	0.5	1.0	11.8
227-11	10.7	Within (S)	18.1	4.5	61.0	4.3	5.2	7.0
227-12	18.7	Within (S)	29.7	10.0	42.3	8.2	1.8	8.0
259-5	5.6	After (N)	34.7	3.0	48.5	0.0	4.7	9.2
230-17	9.0	After (N)	15.3	0.0	53.8	8.2	6.2	16.5
13-Z	15.9	After (N)	26.8	0.0	53.2	0.0	11.9	8.2
230-19	19.6	After (N)	6.6	0.5	21.4	68.0	0.0	3.6
13-Beta	48.4	After (N)	12.1	0.0	41.7	0.0	6.6	39.6

*Domains relative to the fault bend, either north (N) or south (S) of the San Gabriel Fault.

**Other: Clays, unknown opaques, other minerals (biotite, muscovite, hornblende, unknown).

4.3. Fault Zone Description

The North Branch of the San Gabriel Fault has a consistent fault zone structure over the extent of mapping with a distinct fault core (Figures 3 and 11). The fault zone structure observed in the study area is consistent with that described previously along the San Gabriel Fault [e.g., *Anderson et al.*, 1983; *Chester et al.*, 1993; *Evans and Chester*, 1995]. The fault zone structure (Figure 11) contains a principal slip surface (ultracataclasite or gouge layer) that is 2 to 20 cm thick, with an adjacent foliated cataclasite of several meters, and an outer lying damage zone of 30 to 100 m.

Similar to observations from previous studies, the principal slip surface is a dark brown ultracataclasite that is a severely comminuted and indurated aphanitic rock, which can transition into one or more closely spaced, less mature gouge layers in some areas [e.g., *Anderson et al.,* 1983; *Chester et al.*, 1993]. The foliated cataclasite directly adjacent to the principal slip surface is distinctly red or green within the study area [e.g., *Chester et al.*, 1993]. The damage zone is cut by mesoscale to macroscale subsidiary faults, contains patches of weakly to strongly foliated rocks, and often can display abrupt changes in lithology. The larger subsidiary faults reach lengths up to tens of meters, and clearly are associated with a local increase in damage intensity, particularly represented by an increase in small subsidiary fault density. The smaller subsidiary faults range from a few centimeters to several meters in length, the larger of which have their own damage zones that range from a few to tens of centimeters thick.

The macroscopic bend region in the NBSGF is characterized by an abrupt 13° change in strike between two relatively planar, hard-linked fault segments (Figure 12).

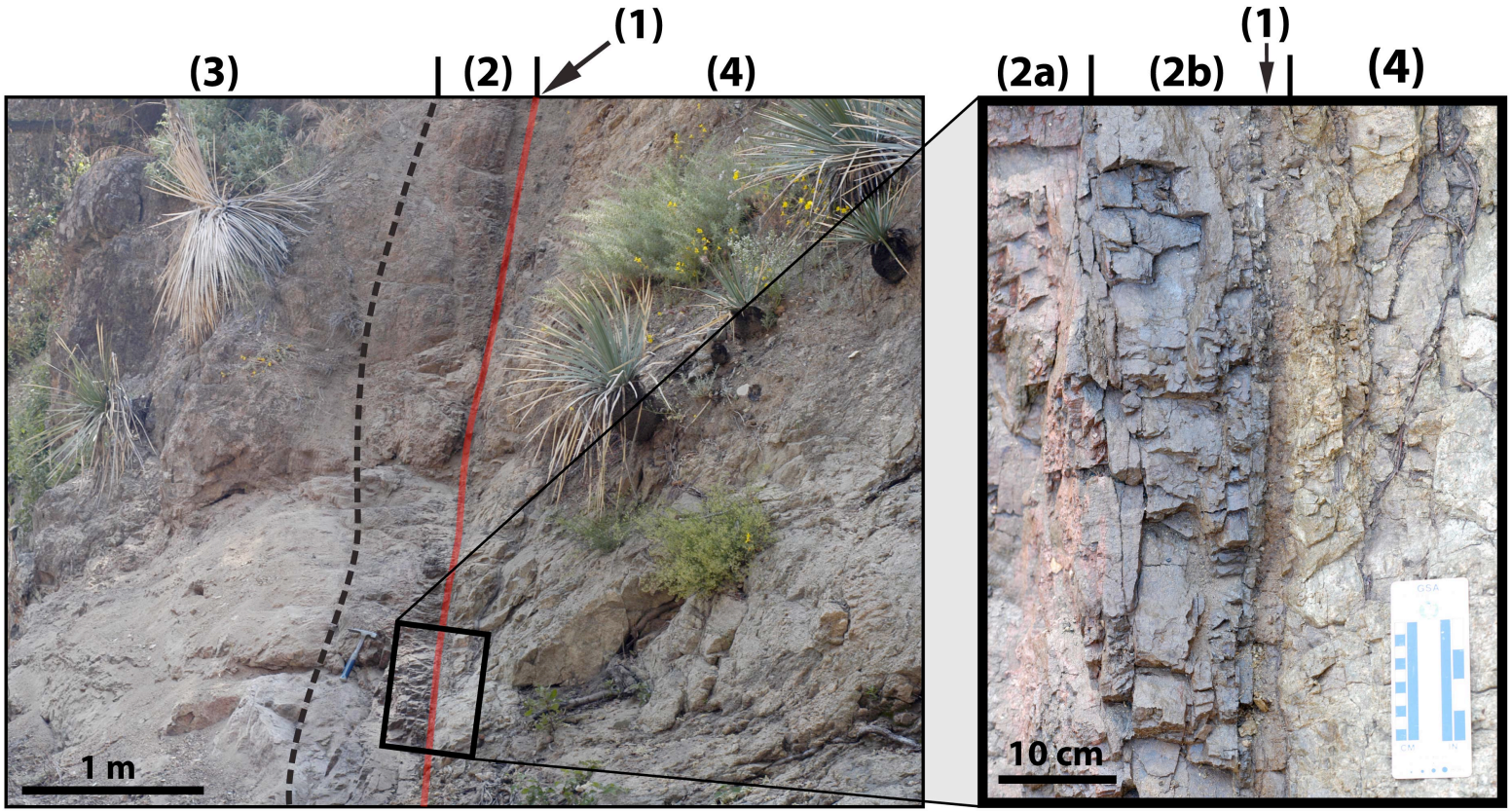

Figure 11. Fault zone photos for the NBSGF. Photo of the fault zone (on left) and fault core (on right) exposed at Station 227 (Figure 10). (1) Principal slip surface, (2a) ultracataclasite layer, (2b) cataclastic red granodiorite, (3) red granodiorite, and (4) tan granodiorite.

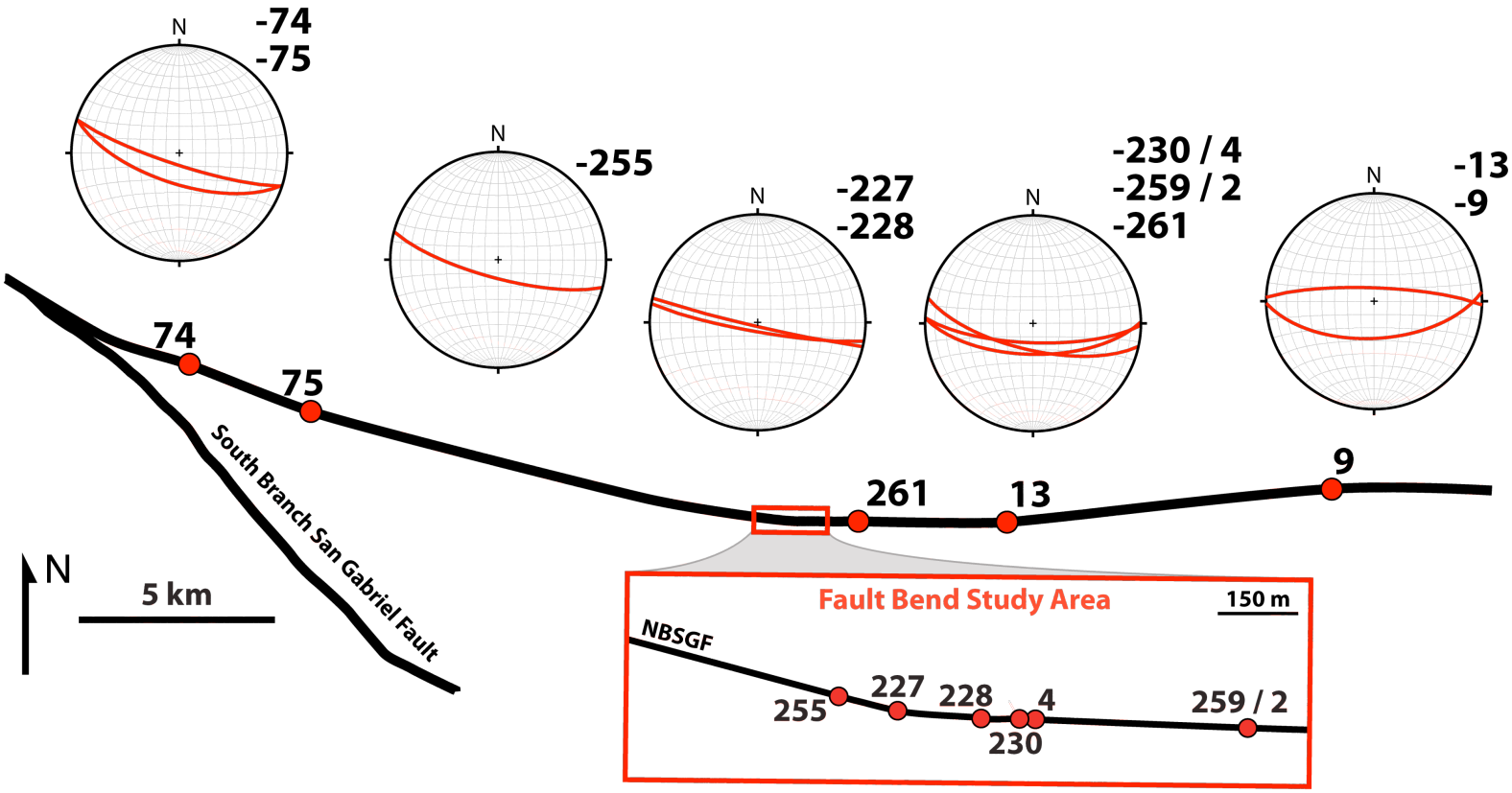

Figure 12. Orientations of the NBSGF. Schematic diagram of the NBSGF through the field area of interest (Figure 3), with the fault bend study area magnified on the bottom. Lower-hemisphere, equal-area stereographic projects with north at the top are displayed above the fault, showing the orientation of the North Branch San Gabriel Fault throughout the field area. Each fault exposure (red dots) corresponds to an average measurement of the fault surface (red great circle) on the stereonet.

The planar segments extend at least 10 km to the west and east, having strikes of 105° and 092°, respectively. A single, continuous fault surface is inferred through the macroscopic bend based on the remote sensing analysis of topography, and the orientation and alignment of five discontinuous, but well-preserved fault core exposures over about 425 m (Figures 9a, 9c, and 12). The excellent exposures of the fault core include four from the current study and one from a previous study [Figure 10b; *Chester and Chester*, unpublished data, 2010].

4.4. Off-fault Damage Characteristics

4.4.1. Mesoscale Linear Subsidiary Fault Density

The linear subsidiary fault density (LSFD) was determined along nine traverses perpendicular, and one traverse approximately parallel, to the NBSGF trace (Table 3; Figures 13-14). The parallel traverse shows that there are significant variations in LSFD closer to the ultracataclasite layer, most likely associated with large subsidiary faults (Figure 14). In general, however, these data show an exponential decrease in LSFD with distance from the ultracataclasite and that the difference in LSFD in each structural domain is not appreciably different (Figure 13).

4.4.2. Intermediate Scale Linear Transgranular Fracture Density

For samples closer to the fault core, the linear transgranular fracture density (LTFD) of fractures 2.5 to 10 mm in length is systematically greater than the LTFD of fractures longer than 10 mm (Tables 4-5; Figures 15-16). In contrast, the LTFD in samples collected more than 20 m from the ultracataclasite show an average 9% decrease (Figure 15). Even though the variation in LTFD becomes more prominent

Table 3.
Mesoscale Linear Fault Density Information

Location	Traverse	Domains*	Measurement Stations	Distance from Fault (m)		Total Traverse Length (m)**
				Start	End	
255	1	After (S)	70	0.3	57.6	87.5
227	2	Within (S)	53	0.2	26.8	63.7
227	3	Within (N)	29	0.1	17.0	33.7
262	4	Within (N)	25	21.1	64.3	92.0
230	5	Before (S)	51	0.3	70.6	96.5
230	6	After (N)	45	0.3	38.6	43.3
259	7	After (N)	73	0.2	40.1	76.7
261	8	After (N)	54	0.3	39.1	54.5
228	9	Within (S)	53	3.8	60.3	81.9
231	10***	Before (S)	43	3.5	11.0	69.6

*Domains relative to the fault bend, either north (N) or south (S) of the San Gabriel Fault.
**Actual length from the beginning to the end of the traverse.
***Fracture density traverse (FDT) measured approximately parallel to the fault trace.

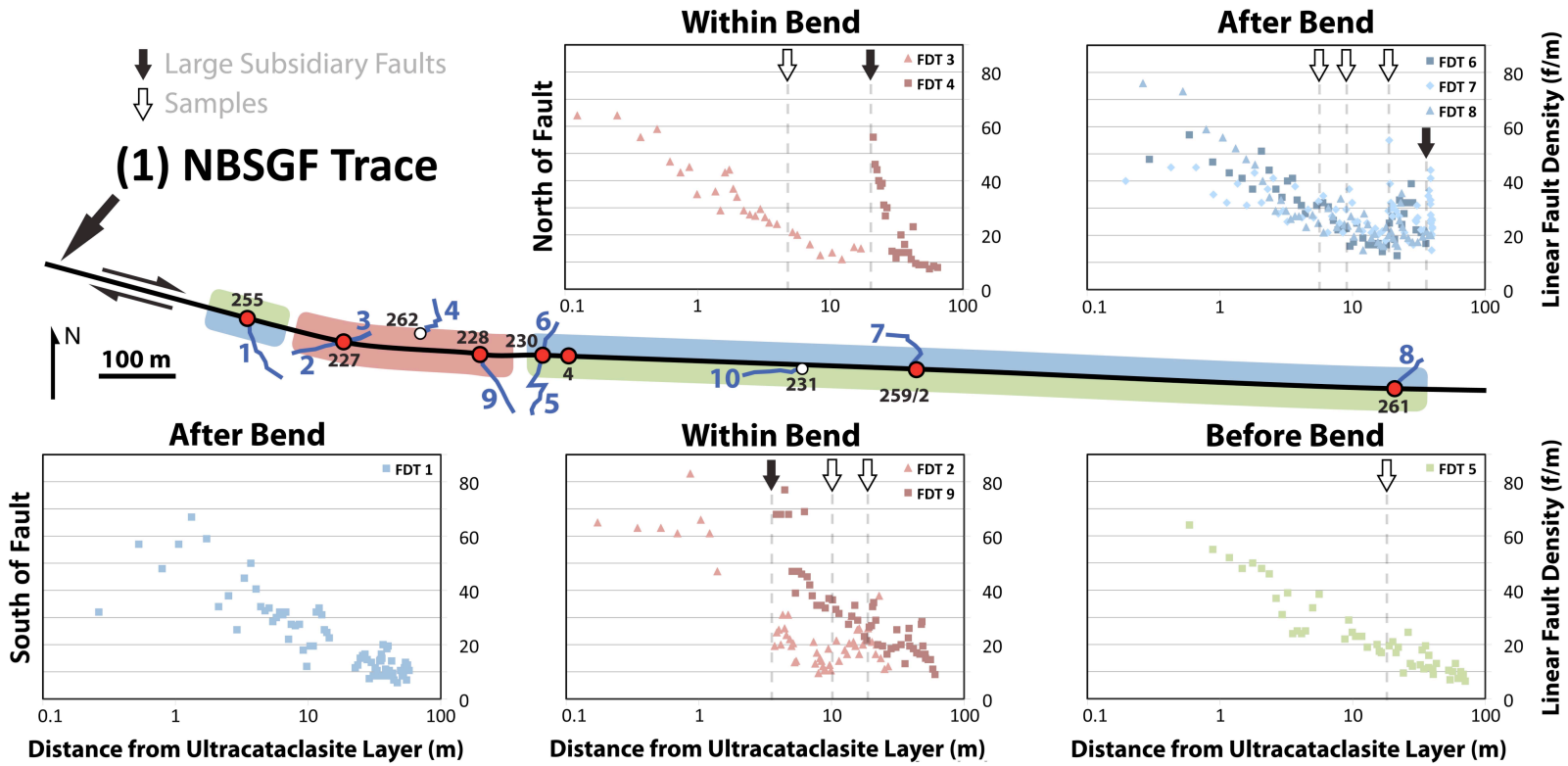

Figure 13. LSFD perpendicular to NBSGF. Plots of the linear subsidiary fault density, displayed as faults per meter (f/m), in the San Gabriel Basement Complex (a-e) as a function of perpendicular distance from the ultracataclasite layer of the NBSGF along nine different traverses (Figure 10b). (1) Schematic diagram of the NBSGF bend showing the relative location of these data along the strike, fault core locations (red), and fracture density traverses (dark blue). Large subsidiary faults (solid) and sampling locations (hollows) are indicated with arrows.

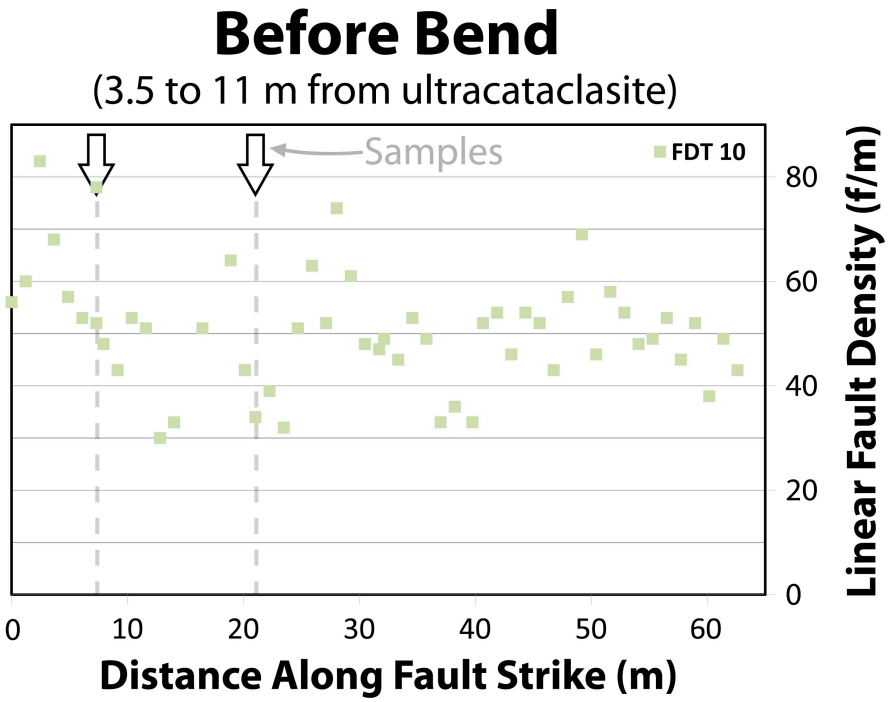

Figure 14. LSFD parallel to NBSGF. Plot of the linear subsidiary fault density, displayed as faults per meter (f/m), south of the NBSGF. Measured at location 231 (Figure 10b) in the San Gabriel Basement Complex running approximately parallel (3.5 to 11 m perpendicular distance) with the ultracataclasite layer of the NBSGF.

Table 4.
Linear Transgranular Fracture Density 10x10mm Grid

Sample	Distance from Fault (m)	Domains*	Linear Microfracture Density (mf/mm)				
			Total	Open	Sealed	Gouge	Cataclastic Zone
231-3[1]	5.4	Before (S)	0.56	0.04	0.29	0.23	0.00
231-2[1]	7.2	Before (S)	0.43	0.01	0.40	0.03	-
13-N[2]	10.1	Before (S)	0.30	0.12	0.07	0.11	-
230-11[1]	17.8	Before (S)	0.43	0.01	0.08	0.35	-
13-Phi[2]	69.2	Before (S)	0.21	0.10	0.08	0.02	0.01
227-9[3]	4.8	Within (N)	0.43	0.24	0.09	0.07	0.03
227-11[3]	10.7	Within (S)	0.56	0.06	0.38	0.12	-
227-12[3]	18.7	Within (S)	0.55	0.01	0.46	0.06	0.02
259-5[1]	5.6	After (N)	0.36	0.05	0.21	0.09	-
230-17[1]	9.0	After (N)	0.65	0.07	0.46	0.11	0.01
13-Z[1]	15.9	After (N)	0.53	0.01	0.36	0.14	0.03
230-19[1]	19.6	After (N)	0.53	-	0.35	0.18	-
13-Beta[1]	48.4	After (N)	0.23	0.05	0.11	0.08	-

*Domains relative to the fault bend, either north (N) or south (S) of the San Gabriel Fault.
[1, 2, 3] - Number of perpendicular thin sections measured for each sample.
mf/mm - Microfracture per millimeter

Table 5.
Linear Transgranular Fracture Density 2.5x2.5mm Grid

Sample	Distance from Fault (m)	Domains*	Linear Microfracture Density (mf/mm)				
			Total	Open	Sealed	Gouge	Cataclastic Zone
231-3[1]	5.4	Before (S)	0.53	0.04	0.25	0.22	0.01
231-2[1]	7.2	Before (S)	0.41	0.01	0.36	0.03	-
13-N[2]	10.1	Before (S)	0.29	0.11	0.07	0.11	-
230-11[1]	17.8	Before (S)	0.45	0.01	0.07	0.37	-
13-Phi[2]	69.2	Before (S)	0.20	0.10	0.07	0.01	0.01
227-9[3]	4.8	Within (N)	0.40	0.22	0.08	0.06	0.03
227-11[3]	10.7	Within (S)	0.51	0.06	0.32	0.13	-
227-12[3]	18.7	Within (S)	0.52	0.01	0.43	0.07	0.01
259-5[1]	5.6	After (N)	0.36	0.06	0.21	0.09	-
230-17[1]	9.0	After (N)	0.55	0.07	0.38	0.09	0.02
13-Z[1]	15.9	After (N)	0.50	0.01	0.34	0.13	0.03
230-19[1]	19.6	After (N)	0.52	-	0.35	0.17	-
13-Beta[1]	48.4	After (N)	0.23	0.04	0.13	0.06	-

*Domains relative to the fault bend, either north (N) or south (S) of the San Gabriel Fault.
[1, 2, 3] - Number of perpendicular thin sections measured for each sample.
mf/mm - Microfracture per millimeter

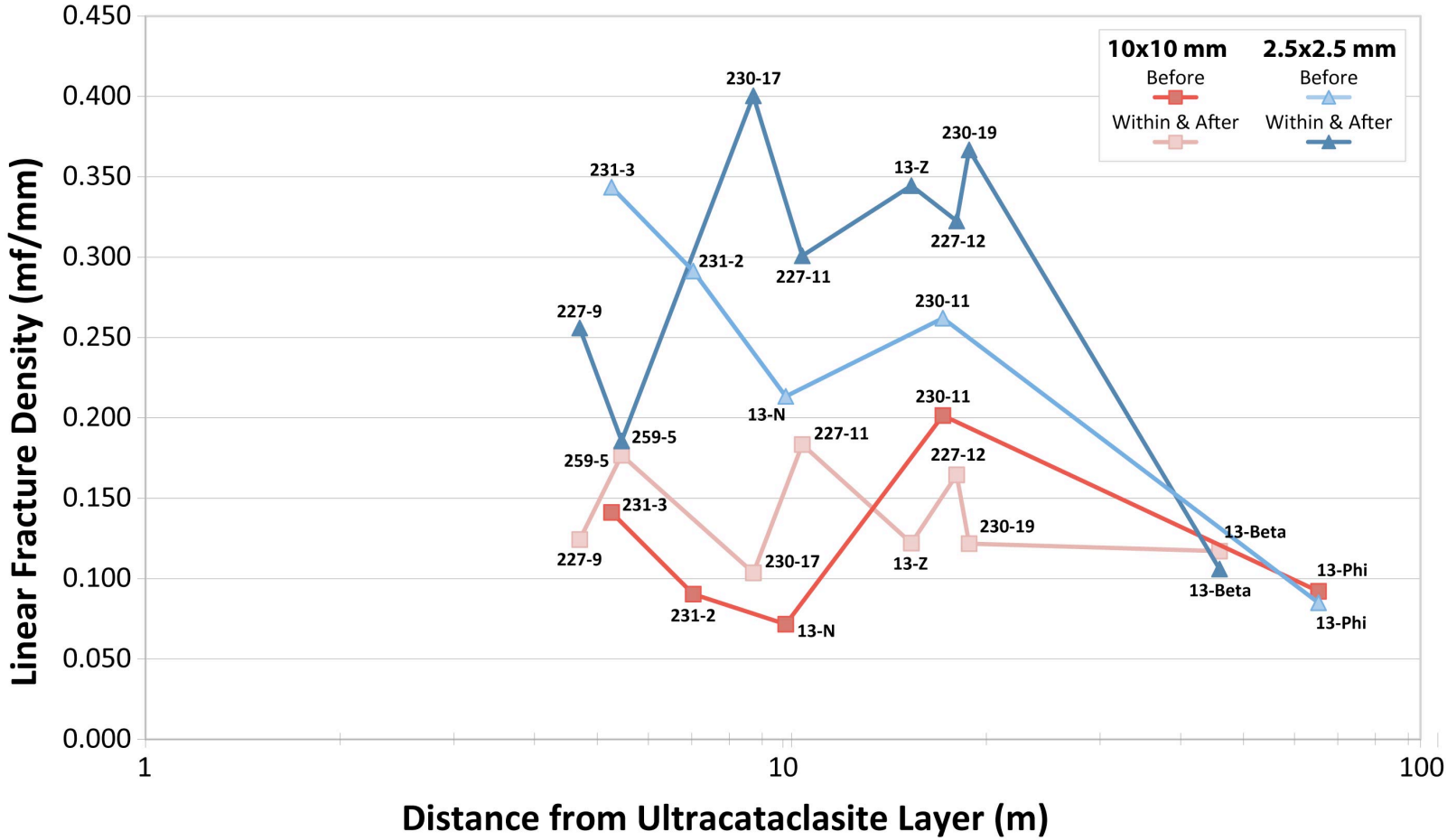

Figure 15. LTFD combined. Linear transgranular fracture density displayed in microfracture per millimeter (mf/mm), with measurements averaged for each sample. Variations in transgranular fracture density as a function of distance (in meters) from the NBSGF ultracataclasite layer. Data are separated into domains before the bend, and combine domains within and after the bend for each grid size (10 mm and 2.5 mm). Transgranular fracture density is measured and averaged for 1 to 3 mutually perpendicular thin sections per sample, located at distances from 4.8 to 69.2 m (Tables 4-5).

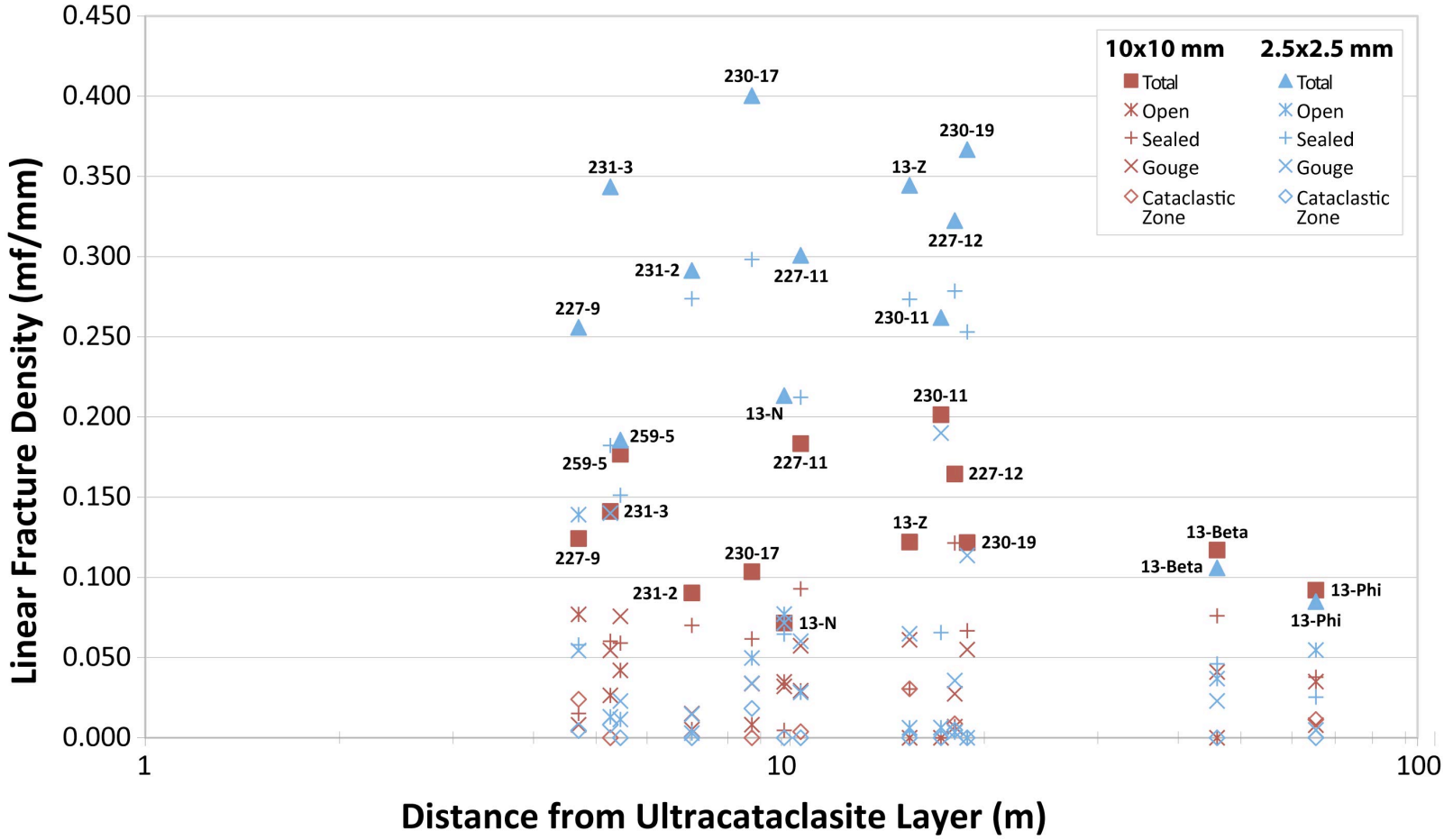

Figure 16. LTFD fracture types. Linear transgranular fracture density displayed in microfracture per millimeter (mf/mm), with measurements averaged for each sample. Variations in transgranular fracture density as a function of distance (in meters) from the NBSGF ultracataclasite layer. Data are separated by grid size (10 mm and 2.5 mm) and fracture type for each sample along with the total fractures (key in upper right). Transgranular fracture density is measured and averaged for 1 to 3 mutually perpendicular thin sections per sample, located at distances from 4.8 to 69.2 m (Tables 4-5).

closer to the ultracataclasite layer, the general trends are essentially the same in each structural domain.

The type of each transgranular fracture is also noted along with the LTFD (Figure 16). The relative proportion of transgranular fracture types is similar in each structural domain. On average, 55.9% of the fractures are sealed, 26.1% are gouge-filled, 16.6% are open, and 1.5% are cataclastic zones.

4.4.3. Linear Intragranular Fracture Density

The linear intragranular fracture density of the quartz grains in most of the samples ranges from 34.2 to 54.1 mf/mm, with one value for sample 227-12 significantly higher at 66.9 mf/mm (Table 6; Figure 17). The LIFD before the bend decreases with distance from the ultracataclasite layer, and the combined data set for samples within and after the bend shows an increase in LIFD with distance from the ultracataclasite (Figure 13). Sample 227-12 is located within the bend and to the south, directly adjacent to a spike in the LSFD; this sample has a LIFD value significantly higher than the general trend (Figure 13).

The LIFD of the feldspar grains is also similar for all samples with values ranging from 22.1 to 35.9 mf/mm, and again, with one significantly higher mf/mm value of 45.7 for sample 227-12 (Table 7; Figure 18). The LIFD in the feldspar grains before the bend is lower than the other samples overall, but shows similar trends within and after the bend. Additionally, the LIFD in the feldspar grains is, for the most part, systematically lower than that of quartz (Figure 19).

Table 6.
Quartz Linear Intragranular Fracture Density

Sample	Distance from Fault (m)	Domains*	# Grains	Linear Microfracture Density (mf/mm)			
				Total	Open	Sealed	Healed
231-3[1]	5.4	Before (S)	69	47.1	1.0	3.9	41.8
231-2[1]	7.2	Before (S)	69	52.1	0.3	7.5	43.7
13-N[2]	10.1	Before (S)	124	34.4	2.9	0.5	30.8
230-11[1]	17.8	Before (S)	44	38.2	5.3	5.2	26.3
13-Phi[2]	69.2	Before (S)	148	34.2	3.9	0.3	29.9
227-9[3]	4.8	Within (N)	135	37.2	5.4	3.5	27.7
227-11[3]	10.7	Within (S)	118	50.3	2.8	3.4	42.7
227-12[3]	18.7	Within (S)	142	66.9	0.9	2.7	62.9
259-5[1]	5.6	After (N)	42	48.9	10.2	3.8	33.2
230-17[1]	9.0	After (N)	42	43.8	16.1	4.8	22.1
13-Z[1]	15.9	After (N)	35	52.0	4.0	1.7	45.2
230-19	19.6	After (N)	-	-	-	-	-
13-Beta[1]	48.4	After (N)	40	54.1	20.7	4.0	28.8

*Domains relative to the fault bend, either north (N) or south (S) of the San Gabriel Fault.
[1, 2, 3] - Number of perpendicular thin sections measured for each sample.

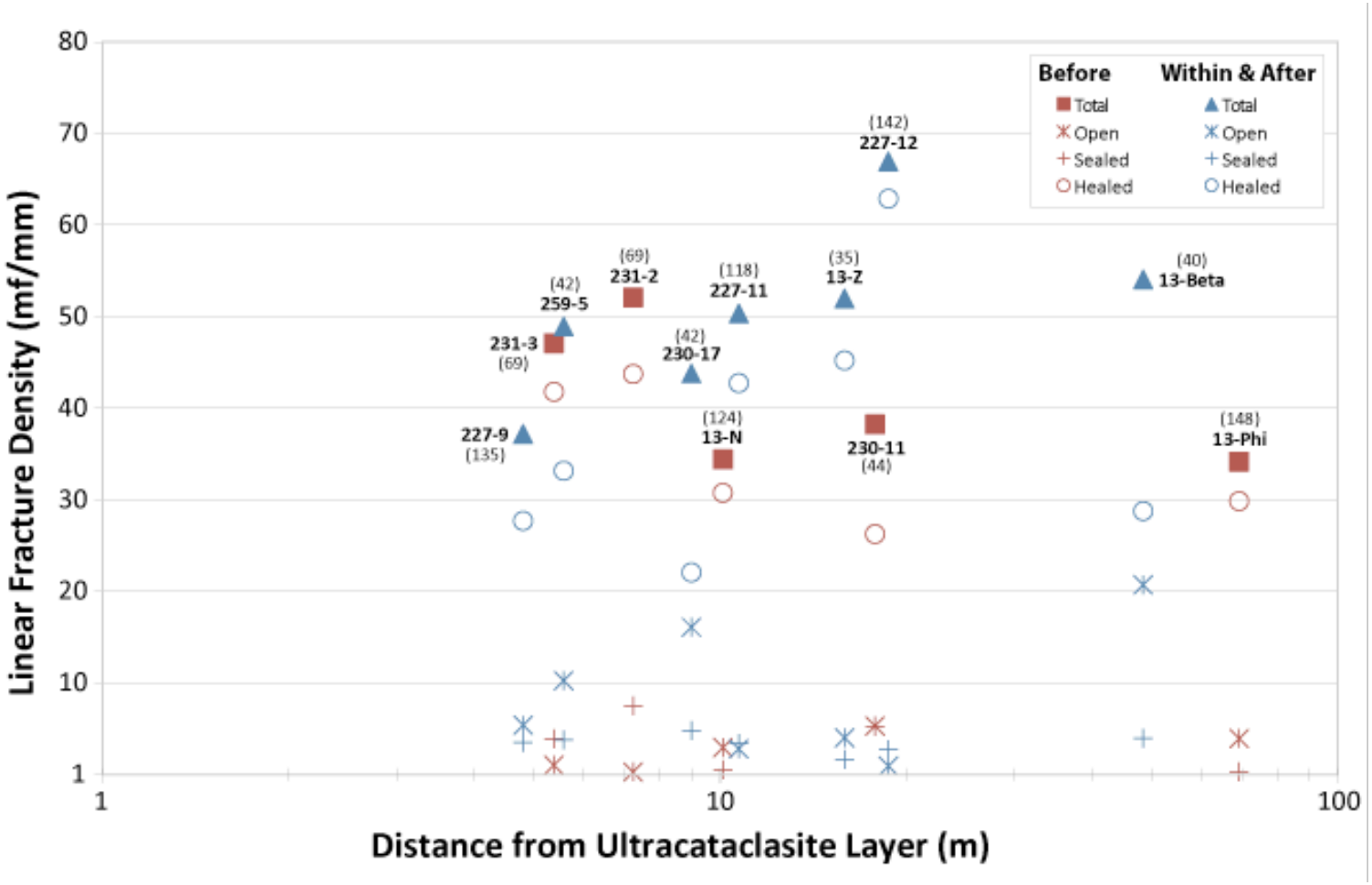

Figure 17. Quartz LIFD fracture types. Quartz linear intragranular fracture density displayed as microfracture per millimeter (mf/mm). Variations in intragranular fracture density as a function of distance (in meters) from the NBSGF ultracataclasite layer. Data are separated by fracture type for each sample including total fractures (key in upper right), and into domains before the bend as well as combine domains within and after the bend. The number of grains measured is indicated in parentheses. Intragranular fracture density is measured in 1 to 3 mutually perpendicular thin sections that are averaged for each sample, located at distances from 4.8 to 69.2 m (Tables 6-7).

Table 7.
Feldspar Linear Intragranular Fracture Density

Sample	Distance from Fault (m)	Domains*	# Grains	Linear Microfracture Density (mf/mm)			
				Total	Open	Sealed	Healed
231-3[1]	5.4	Before (S)	1	-	-	-	-
231-2[1]	7.2	Before (S)	3	28.1	0.0	19.6	8.5
13-N[2]	10.1	Before (S)	21	26.1	16.8	1.6	7.8
230-11[1]	17.8	Before (S)	30	22.1	6.7	7.9	7.4
13-Phi[2]	69.2	Before (S)	3	34.5	9.1	0.0	25.4
227-9[3]	4.8	Within (N)	42	32.4	11.8	3.0	17.5
227-11[3]	10.7	Within (S)	91	30.3	4.4	5.1	20.8
227-12[3]	18.7	Within (S)	13	45.7	1.1	11.0	33.6
259-5[1]	5.6	After (N)	24	25.9	10.5	4.0	11.4
230-17[1]	9.0	After (N)	15	25.2	12.3	7.1	5.7
13-Z[1]	15.9	After (N)	33	35.9	22.2	2.2	11.4
230-19	19.6	After (N)	-	-	-	-	-
13-Beta[1]	48.4	After (N)	17	29.9	9.5	1.6	18.8

*Domains relative to the fault bend, either north (N) or south (S) of the San Gabriel Fault.
[1, 2, 3] - Number of perpendicular thin sections measured for each sample.

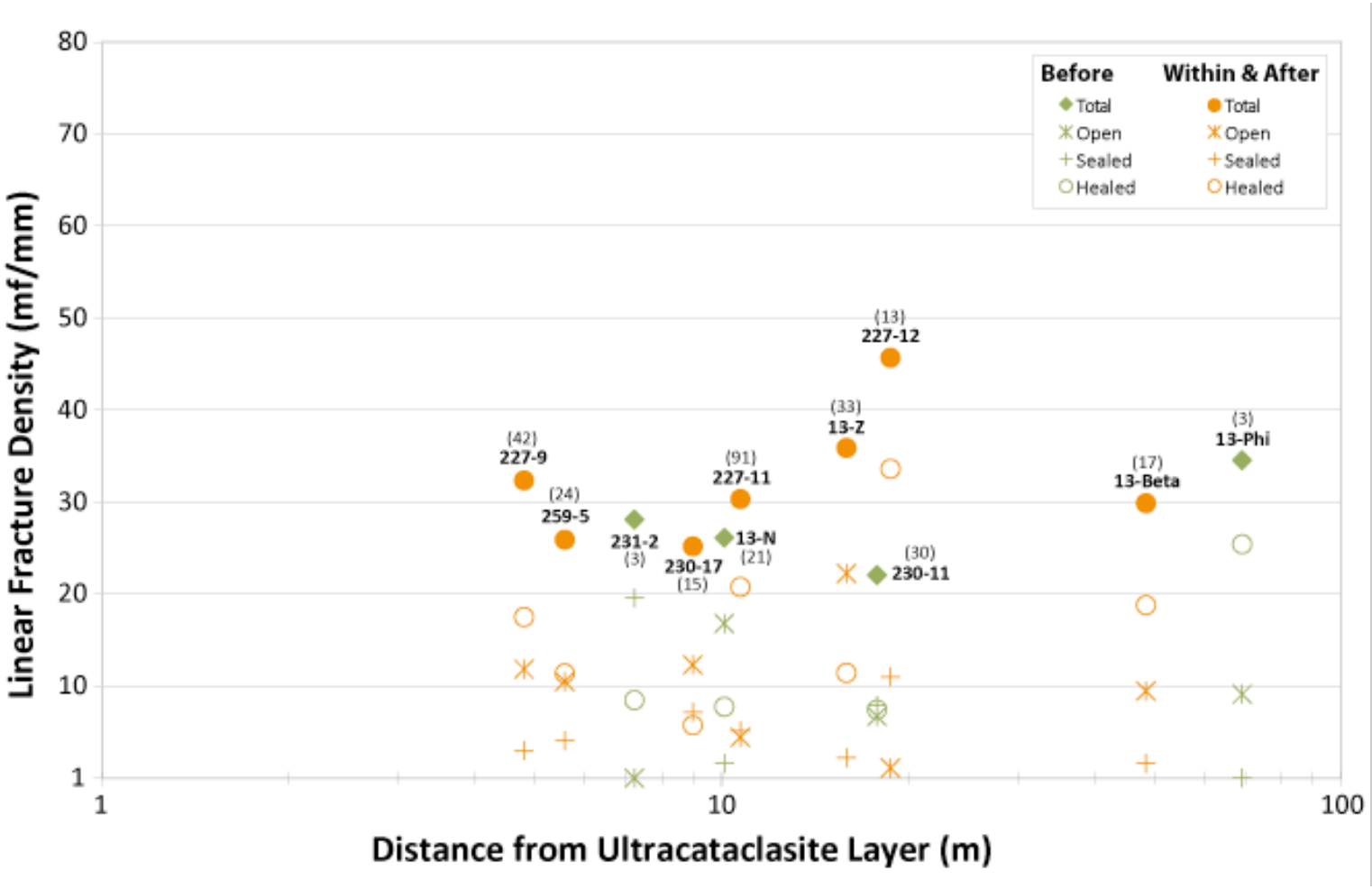

Figure 18. Feldspar LIFD fracture types. Feldspar linear intragranular fracture types displayed as microfracture per millimeter (mf/mm). Variations in intragranular fracture density as a function of distance (in meters) from the NBSGF ultracataclasite layer. Data are separated by fracture type for each sample including total fractures (key in upper right), and into domains before the bend as well as combined domains within and after the bend. The number of grains measured is indicated in parentheses. Intragranular fracture density is measured in 1 to 3 mutually perpendicular thin sections that are averaged for each sample, located at distances from 4.8 to 69.2 m (Tables 6-7).

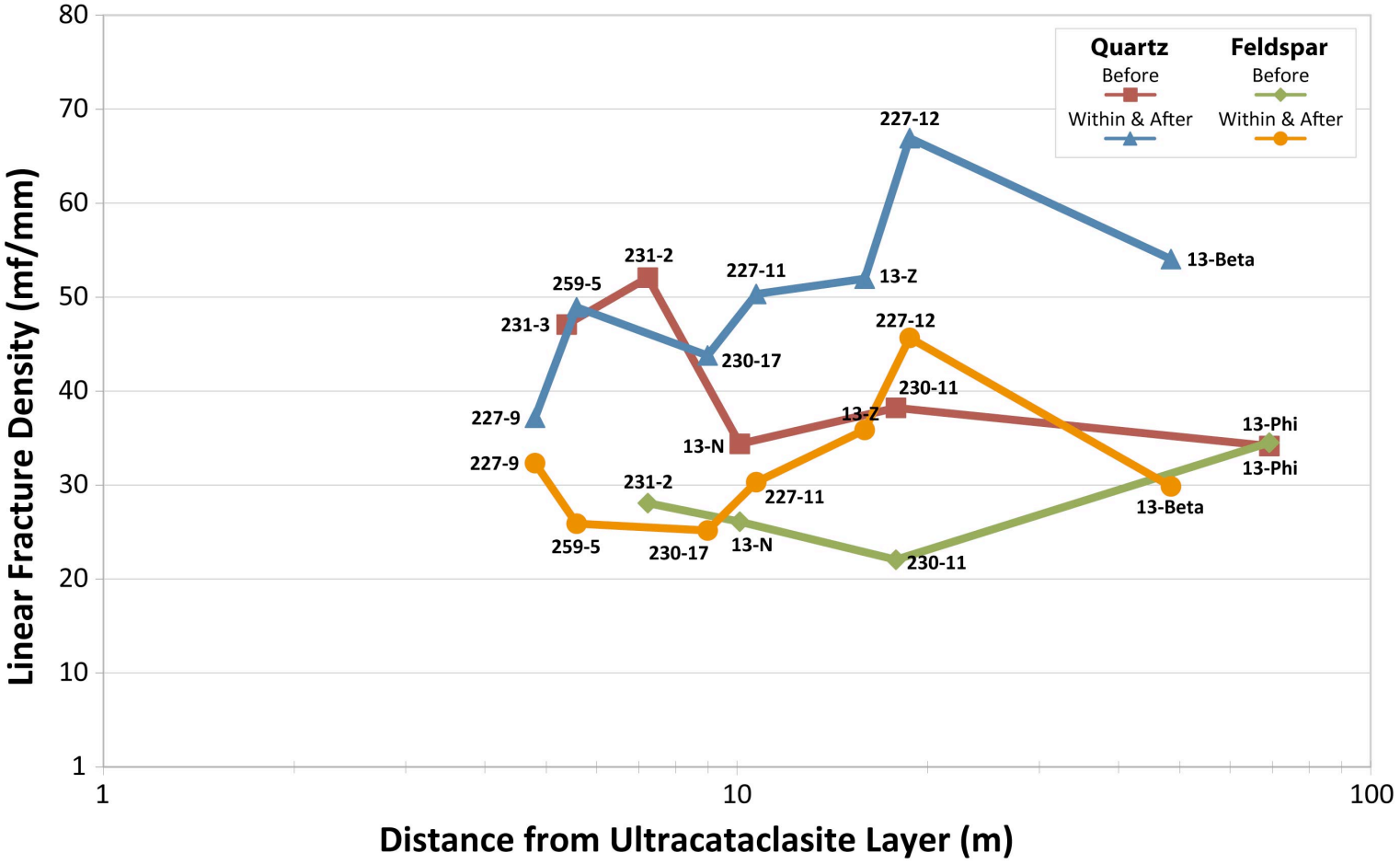

Figure 19. LIFD combined. Linear intragranular fracture density displayed as microfractures per millimeter (mf/mm). Variations in intragranular fracture density as a function of distance (in meters) from the NBSGF ultracataclasite layer. Data are separated into domains before the bend, and combined domains within and after the bend. Intragranular fracture density is measured in 1 to 3 mutually perpendicular thin sections that are averaged for each sample, located at distances from 4.8 to 69.2 m (Tables 6-7).

On average, in quartz 82.3% of the fractures are healed, 9.8% are open, and 7.9% are sealed, and in feldspar 46.0% of the fractures are healed, 36.5% are open, and 17.5% are sealed (Figures 17-18). Even though the fracture type proportions for quartz and feldspar are significantly different, the relatively proportions of the average fracture types in both quartz and feldspar grains is similar in each structural domain.

4.4.4. Mesoscale Subsidiary Fault Orientations

This study presents subsidiary fault orientations adjacent to the macroscopic bend combined with unpublished and published data acquired along the straighter segment of the fault to the east and west of the bend [*Chester et al.*, 1993; *Chester and Chester*, unpublished data, 2010]. The orientations of 582 subsidiary faults were recorded at 37 stations. Slip-lineations were measured on 476 of these subsidiary fault surfaces (Figure 20). Although the number of orientations is sparse in some regions, the data are sufficient to show the basic fabric and kinematic trends.

The fabric and kinematics of mesoscale subsidiary faults north and south of the NBSGF are similar along the eastern segment (Figure 20). The fault planes east of the bend are dominantly oriented subvertical and form a quasi-conjugate geometry, which is more prominently displayed in the data south of the fault. The slip lineations and b-axes on both sides of the fault indicate that the faults exhibit mostly strike-slip kinematics. Furthermore, subhorizontal fault planes are nearly absent this data set (Figure 20).

The mesoscale subsidiary fault fabric and kinematics north of the fault, within the bend, show two dominant sets of subsidiary faults (Figure 20). The first set is characterized by subhorizontal faults with highly variable slip-directions. The second set

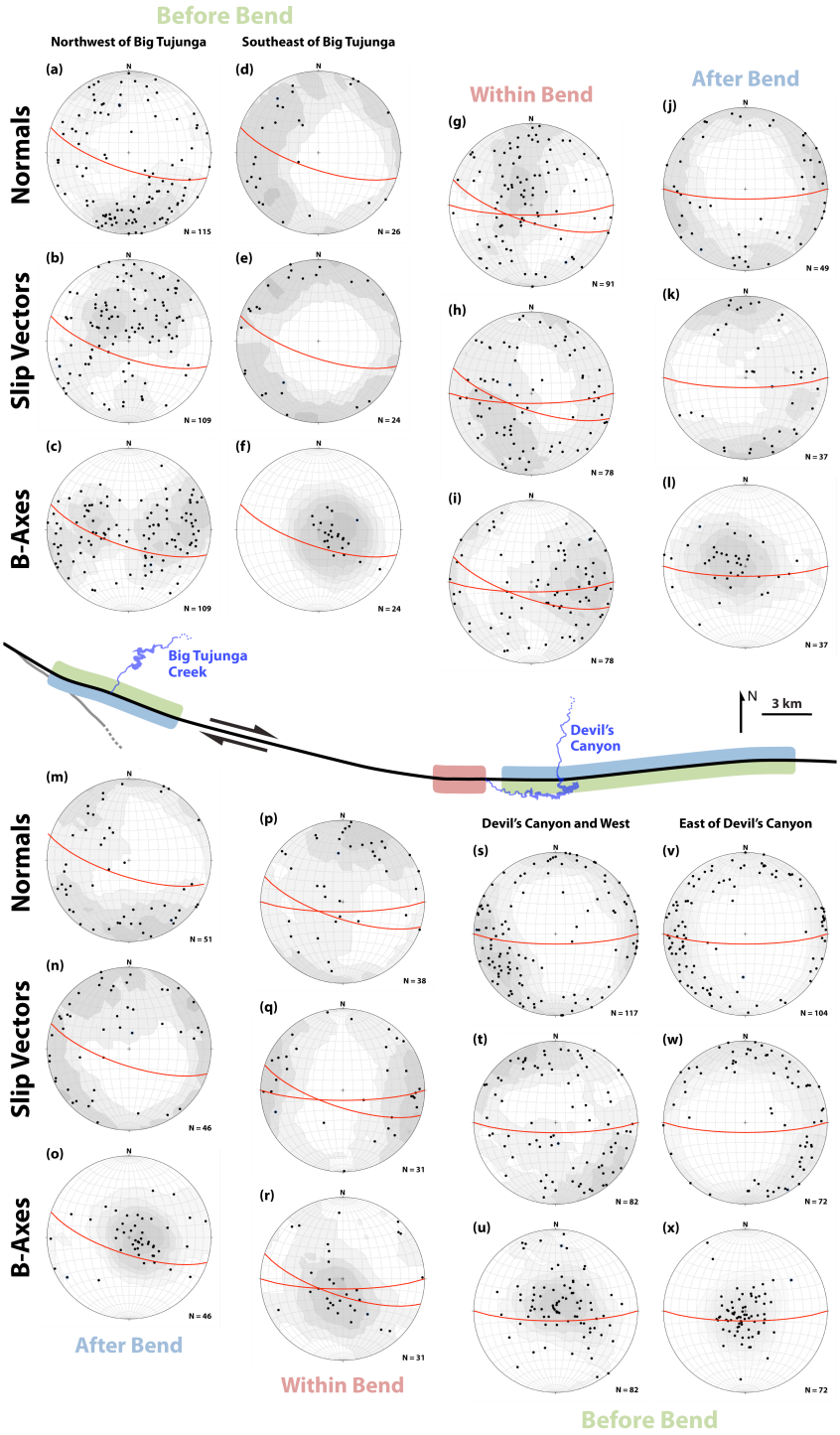

Figure 20. Subsidiary fault orientations and kinematics. Equal-area, lower-hemisphere stereonet projections of poles, slip lineations, and b-axes to subsidiary faults in the NBSGF damage zone, with north at the top and the average NBSGF orientation (great circles). A schematic diagram (middle) shows the relative position of the data located in the domains before (green), within (red), and after (blue) the fault bend.

is northwest striking and subvertical; the slip lineations and b-axes at this location also indicate a highly variable slip-direction (Figure 20). The fabric and kinematics of the mesoscale subsidiary faults within the bend and south of the fault show a dominant set of faults that are subparallel to the NBSGF. These faults display strike-slip kinematics based on the slip lineations and b-axes. A secondary set of subhorizontal faults is also present. The slip lineations and resulting b-axes on the subhorizontal faults indicate mostly strike-slip motion (Figure 20).

The fabric and kinematics of the mesoscale subsidiary faults on the linear segment west of the bend show significant differences north and south of the fault (Figure 20). The fabric north of the fault is dominated by two steeply dipping, northeast-striking fault sets. One set dips steeply to the north with slip lineations and b-axes indicating mostly dip-slip motion. The second set is more variable in dip-direction, and based on the slip lineations and b-axes, displays mostly dip-slip motion (Figure 20). On the south side of the fault to the west of the bend, the mesoscale subsidiary fault fabric and kinematics show two subvertical sets of what appears to be a quasi-conjugate geometry. The slip lineations and b-axes indicate that these two sets display strike-slip kinematics (Figure 20). There are no subhorizontal faults to the west and south of the bend in the NBSGF (Figure 20).

4.4.5. Transgranular Shear Fracture Orientations

The transgranular fracture orientations (TFO) were determined at the thin section scale from 13 samples with one to three mutually perpendicular thin sections per sample. The TFO measurements cover a wide range of distances relative to the fault

(Table 8; Figure 21). The samples illustrate significant variations in lithology along strike and with distance perpendicular to the fault, and display preexisting damage, such as foliations [Figure 21; *Anderson et al.*, 1983]. There are a few strong concentrations in some of the samples, but mostly the fracture orientations define weak to moderate concentrations (Figure 21).

The samples used for the TFO measurements are located in the structural domains within the bend and along the eastern linear segment of the fault (Figure 21). The fabric along the eastern linear segment to the north is characterized by two weak concentrations of subvertical transgranular fractures. One set is oriented at a high angle to the NBSGF and the other set is approximately parallel to the fault (Figure 21e-f). The fabric south of the eastern linear segment exhibits a steeply dipping fault set parallel to the NBSGF, and also the distinct presence of subhorizontal faults (Figures 21l-m). Within the bend, north and south of the fault, the fracture fabric is similar (Figures 21a-d and 21g-j). Many of the samples exhibit a subvertical set that is parallel to the NBSGF, similar to the set seen along the linear segment to the east. Additionally, there are faults striking both northeast and northwest, with dips ranging from subvertical to steeply dipping (Figures 21a-d and 21g-j). The samples located directly adjacent to the fault bend all show subhorizontal faults (Figures 21a, 21g, and 21h). Conversely, those samples located in the same domain within the bend, but at a greater distance from the localized bend, exhibit almost exclusively subvertical faults (Figures 21b-d, and 21i-k)

Table 8.
Transgranular Fracture Fabric Information

Sample	Distance from Fault (m)	Domains*	n	Fracture Type	Concentration
13-N[2]	10.1	Before (S)	44	-	-
13-Phi[2]	69.2	Before (S)	22	O, S	weak
227-9[3]	4.8	Within (N)	97	O, G	moderate
				S, O, G, CZ	weak
259-5[1]	5.6	Within (N)	17	-	-
230-17[1]	9.0	Within (N)	36	S, G, CZ, O	weak
				S, O	moderate
230-19[1]	19.6	Within (N)	49	S, G	moderate
231-3[1]	5.4	Within (S)	47	S, G, O	weak
				S, G, O, CZ	weak
231-2[1]	7.2	Within (S)	51	S, O	moderate
227-11[3]	10.7	Within (S)	131	S, G, O	moderate
				S	strong
230-11[1]	17.8	Within (S)	33	G, O	weak
				G, O	weak
227-12[3]	18.7	Within (S)	133	S, G, O	moderate
				S	moderate
13-Z[1]	15.9	After (N)	41	S, G	weak
				S, G	moderate
13-Beta[1]	48.4	After (N)	18	S, G, O	weak

*Domains relative to the fault bend, either north (N) or south (S) of the San Gabriel Fault.
**F = fractures aligned parallel to foliations
[1, 2, 3] - Number of perpendicular thin sections measured for each sample.
S = sealed; G = gouge; CZ = cataclastic zone; O = open

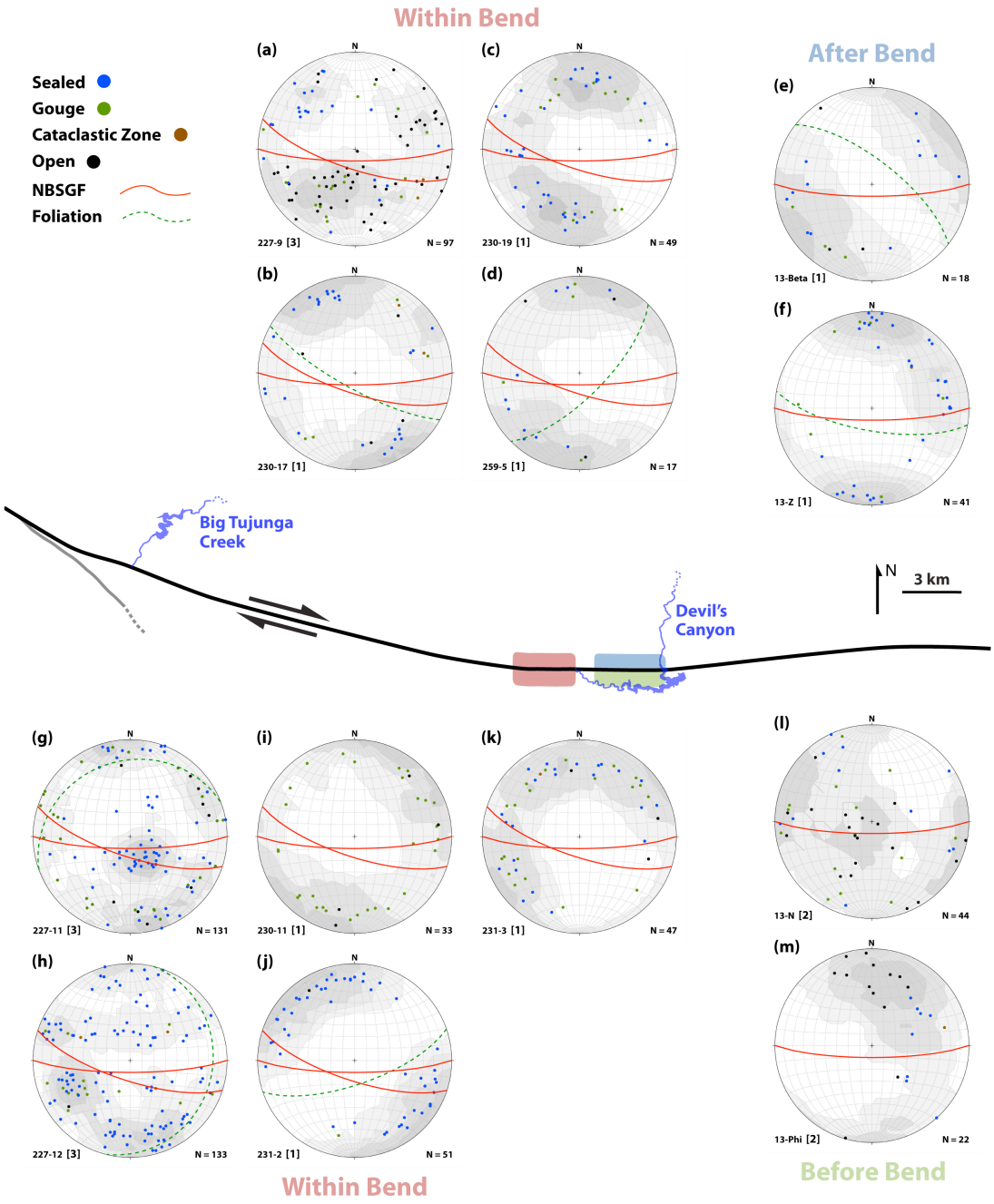

Figure 21. Transgranular fracture orientations. Equal-area, lower-hemisphere stereonet projections of poles microscale transgranular fractures in the NBSGF damage zone (Table 8), with north at the top and planes showing the average orientation of key features (upper left). The thin section name with the number of perpendicular thin sections used is indicated in brackets (on right). A schematic diagram (middle) shows the relative position of the data located in the domains before (green), within (red), and after (blue) the fault bend (Figure 7). Contouring is done using the Kamb method with a contour interval of 2 sigma.

5. DISCUSSION

5.1. Characterization of the Bend in the NBSGF

5.1.1 Macroscopic Geometry of the Fault Trace

The analysis completed on the multispectral imagery and digital elevation models shows the possible presence of a series of hundreds-meter scale, isolated geometric irregularities in the fault surface of the NBSGF (Figure 9a and 9c). The geometric features were not evident when checked in the field, partly because the resolution in the field is limited by variable outcrop size, and extensive soil and alluvium cover. The small-scale topographic features imaged along the NBSGF trace could simply be erosional features having little to do with the actual fault trace. Thus, although there may be some geometric irregularities, none could be observed directly. Furthermore, the orientations of the fault surface, measured directly at exposures of the fault core, are consistent with a simple, smooth change in the fault orientation between outcrops. There is no evidence of isolated, abrupt changes in the orientation of the fault surface, or outcrop-scale bends, kinks, or linking structures.

At the macroscopic scale, the orientation of the fault trace determined from analysis of multispectral imagery and digital elevation models, in conjunction with fault orientations measured in outcrops, support the presence of the isolated, large-scale fault bend in the NBSGF. These data also indicate that the fault is continuous through the bend and along the bounding segments.

Continuous fault surfaces are known to be non-planar at all scales and follow scaling rules [e.g., *Power & Tullis*, 1991; *Sagy & Brodsky*, 2009]. The roughness, however, is characterized by very low amplitude, relative to wavelength, and is not always obvious. This geometric roughness is expected to exist everywhere along the fault surface, and is distinct from the large, isolated and abrupt bend documented at the macroscopic scale within the study area.

5.1.2. Stress and Strain Perturbations Associated with the Bend in the NBSGF

Analytical numerical solutions have shown that, adjacent to a geometric irregularity in the surface of a fault, the stress state becomes non-uniform relative to a linear segment of that fault [e.g., *Chester and Fletcher,* 1997; *Saucier et al.,* 1992]. The size of the stress perturbation scales with the scale of the geometric irregularity. This condition results in a heterogeneous stress state along the fault. An isolated, macroscopic bend like the one observed in the NBSGF, however, should produce a distinct stress perturbation when compared to relatively straight segments. Moreover, the stress field adjacent to an isolated geometric irregularity will become increasingly non-uniform when subjected to the passage of repeated earthquake ruptures [e.g., *Duan and Day,* 2007].

The NBSGF has accommodated significant (16 to 21 km) displacement, and is presumed to have hosted numerous repeated earthquake ruptures over its history. Consequently, the large isolated bend that has a small radius of curvature, specifically a 13° change in strike over about 425 m, is assumed to have produced a significantly perturbed stress state during fault activity (Figure 10). Movement of fault blocks past

such an asperity should have resulted in an increased magnitude of stress and strain within the fault damage zone over and above the variation expected along the bounding straight segments. Furthermore, the perturbation should have produced a significantly different subsidiary fault fabric as the damage zone moved into and out of the bend region.

5.2. Effects of the Fault Bend on the Fault and Fracture Fabric within the NBSGF Damage Zone

5.2.1. Linear Density in the NBSGF Damage Zone

Previous studies conducted along faults of varying levels of maturity show that the rate at which new damage accumulates is not constant, but instead starts high and decreases with increasing fault displacement [e.g., *Chester and Chester*, 1998; *Vermilye and Scholz*, 1998; *Sagy and Brodsky*, 2009; *Faulkner et al.*, 2010, 2011; *Savage and Brodsky*, 2011]. Recent work and data compilations suggest that after a displacement on the order of a km, the thickness of the damage zone remains constant or only increases a small amount [*Faulkner et al.*, 2010, 2011; *Savage and Brodsky*, 2011]. Many studies assert that the linear density of brittle deformation features at the meso- and micro-scale can be best fit by a linear function of the logarithm of distance [e.g., *Anders and Wiltschko*, 1994; *Chester et al., 2005*]. Accordingly, we hypothesize that the damage magnitude is saturated in the large displacement, mature NBSGF. To first order approximation, the mesoscopic scale damage documented in the several traverses of the present study appears to be consistent with the log-distance functional form.

The linear fault and fracture density associated with the NBSGF shows significant changes at the local scale, which may be a product of variations in lithology or the effects of larger subsidiary faults present in the damage zone. Despite the variations, general trends similar to those found in other studies can be interpreted from the density data. The LSFD exhibits a decrease in density with distance from the ultracataclasite layer, which is best fit by a logarithmic function (Figure 22). There is also little change in the general trend in the different structural domains, which directly supports our hypothesis that the steady state damage magnitude is not increased at the large geometric bend (Table 9; Figure 13).

The LTFD data collected from hand samples using a 2.5 mm counting grid shows a similar trend to the LSFD; however, the remaining microscale linear density data show significantly different trends when compared to the mesoscale data (Figure 23). For example, the LTFD data collected on a 10 mm grid and the LIFD data all show a nearly constant trend with distance from the fault.

The linear subsidiary fault, transgranular fracture, and intragranular fracture density data from the current study all show significantly shallower trends than the meso- and micro-scale data from *Chester et al.* [2005] (Figure 24). A recent study by *Savage and Brodsky* [2011] asserts that the dominant processes by which damage accumulates changes with increasing displacement. Additionally, as a fault matures, the enhanced activation of subsidiary faults increases variation in fault and fracture density by causing spikes in the general trend. Consequently, the general linear density trend

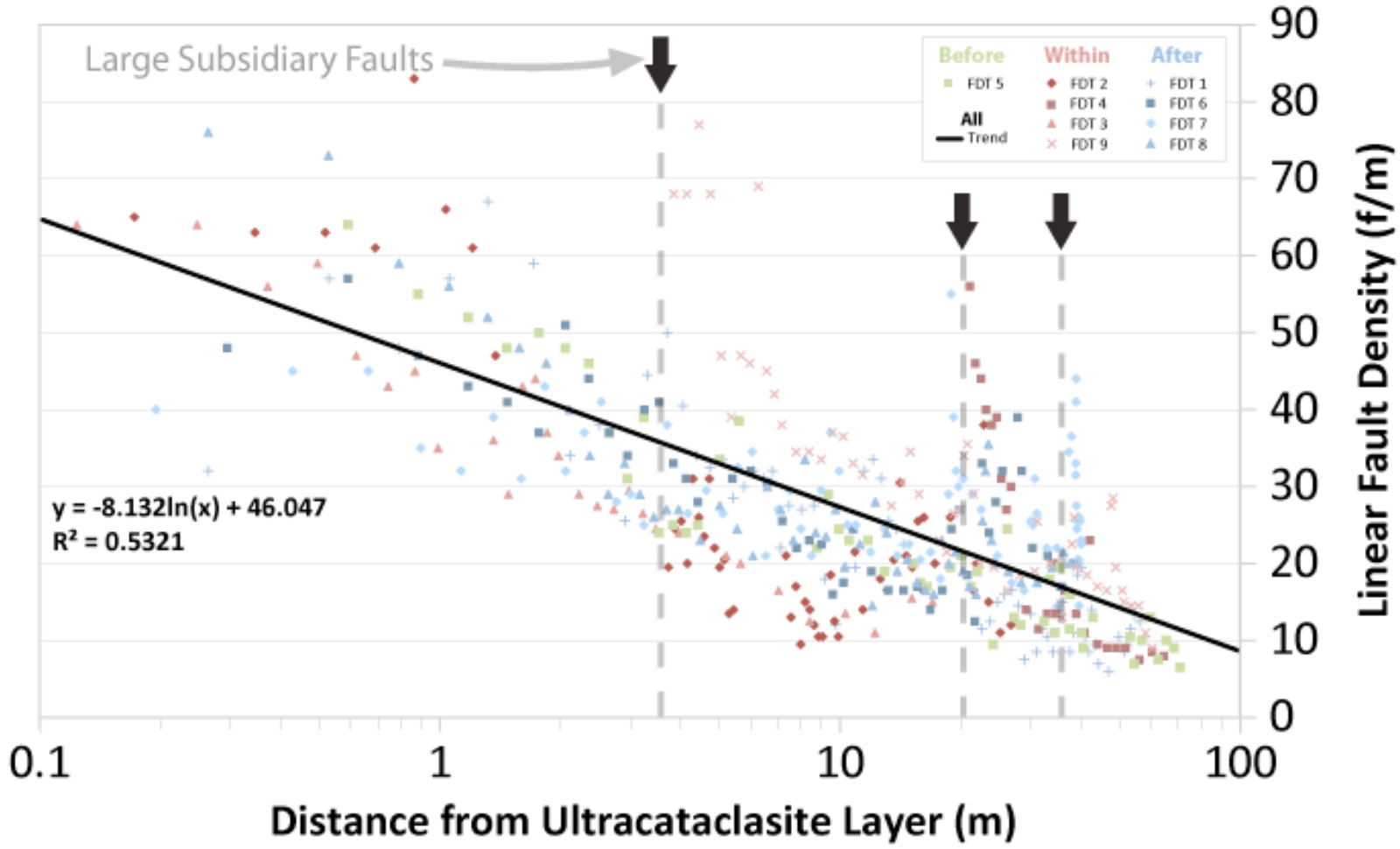

Figure 22. LSFD combined. Linear subsidiary fault density displayed in faults per meter (f/m) as a function of perpendicular distance from the ultracataclasite layer of the NBSGF along nine different traverses (Figure 10b). Each domain is separated by color, and the combined data is fit by a logarithmic function displayed along with the correlation coefficient (R^2) on the left.

Table 9.
Linear Fault and Fracture Density of Mature Faults

Fault	Fault Offset (km)	Depth of Faulting	Fault or Fracture Type	n	R^2 (Power Law)	R^2 (Logarithmic)	Reference
NBSGF	16-21	~3 km	Mesoscale	0.29	0.504	0.532	Current Study
NBSGF	16-21	~3 km	Transgranular (10 mm)	0.05	0.020	0.021	Current Study
NBSGF	16-21	~3 km	Transgranular (2.5 mm)	0.36	0.390	0.259	Current Study
NBSGF	16-21	~3 km	Intragranular (quartz)	0.01	0.001	0.001	Current Study
NBSGF	16-21	~3 km	Intragranular (feldspar)	0.07	0.091	0.090	Current Study
SGF*	16-21	~3 km	Mesoscale	0.23	0.360	0.310	*Chester et al.* [2004]
Arava	105	>3 km	Mesoscale	0.37	0.330	0.450	*Janssen et al*. [2004]
Punchbowl	40	2-4 km	Mesoscale	0.40	0.380	0.510	*Chester and Logan* [1986] and *Wilson et al.* [2003]
Kern Canyon	15	not reported	Mesoscale	0.53	0.800	0.680	J. S. Chester (final technical report, 2001) USGS Annual Project Summary

Table modified from *Savage and Brodsky* [2011].
R^2 - Correlation coefficient.
*Data from previous study along the San Gabriel Fault.
Power law equation $d = cr^{-n}$ used by *Savage and Brodsky* [2011]

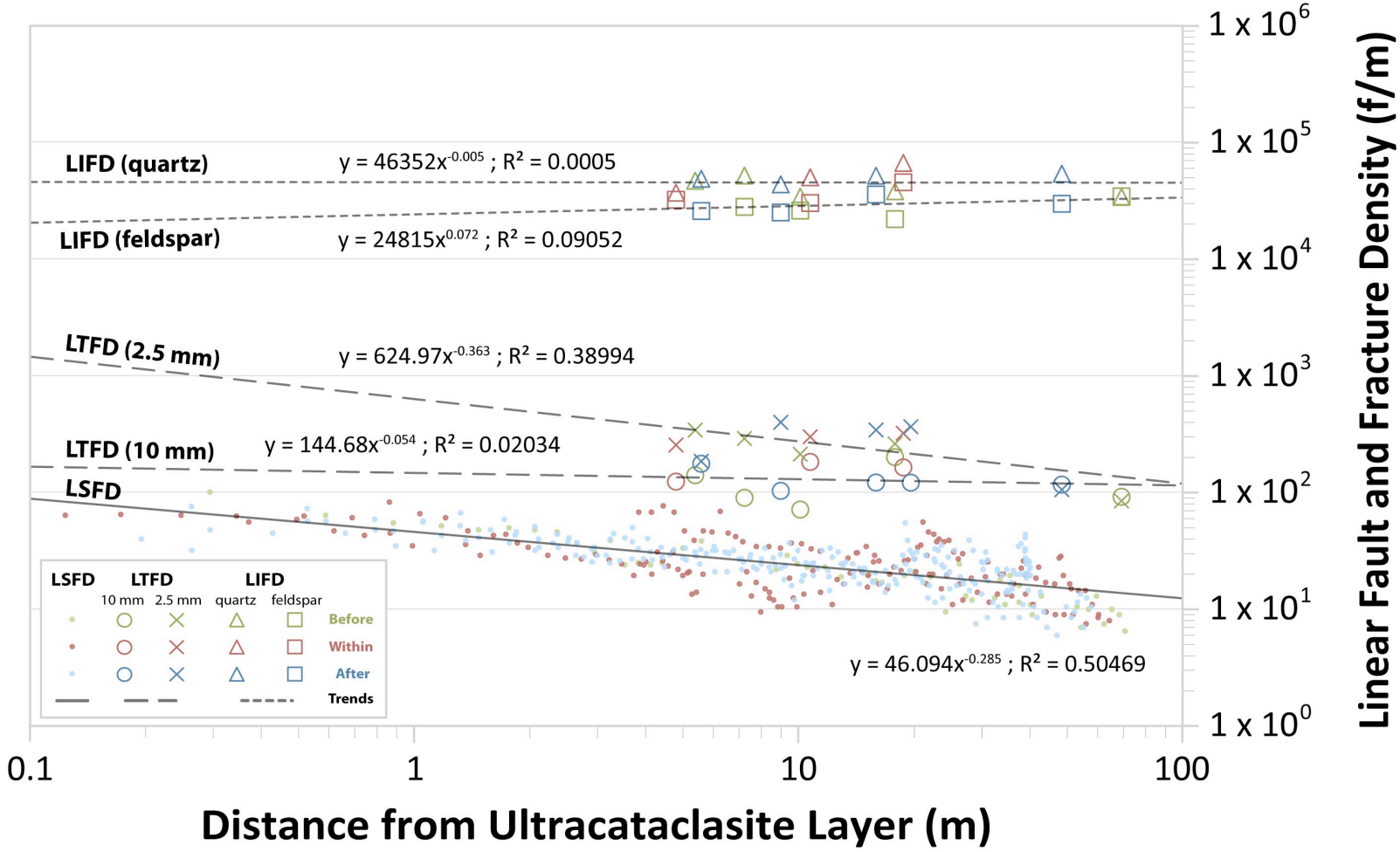

Figure 23. Linear density data combined. Displayed in faults or fractures per meter (f/m) as a function of perpendicular distance from the ultracataclasite layer of the NBSGF. The combined data for linear subsidiary fault density (LSFD), linear transgranular fracture density (LTFD) measured at two scales (10 mm and 2.5 mm), and linear intragranular fracture density (LIFD) measured in quartz and feldspar grains are each fit with a power law function shown along with the corresponding correlation coefficient (R^2).

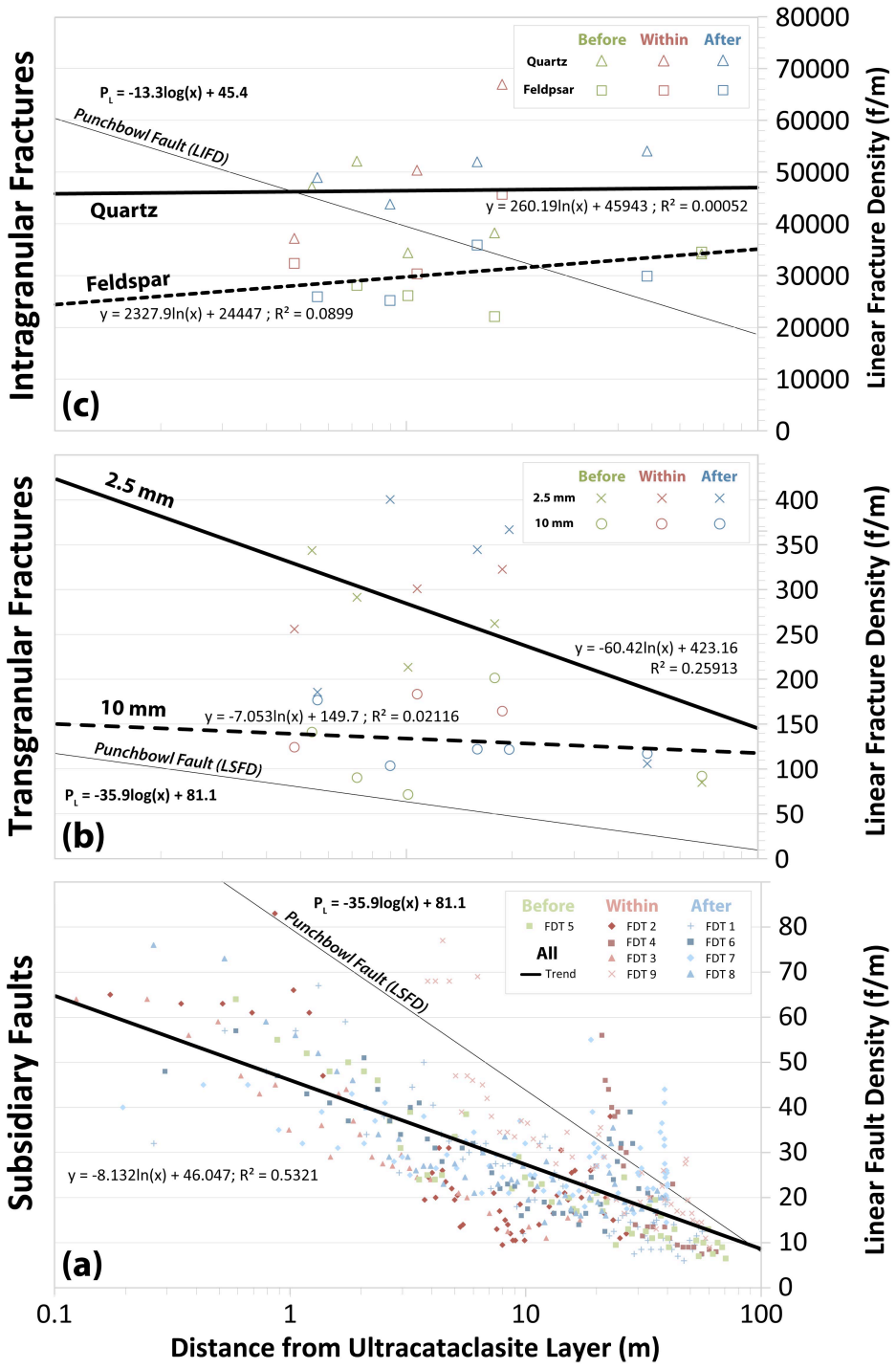

Figure 24. Linear density data compared to Punchbowl Fault. Displayed in faults or fractures per meter (f/m) as a function of perpendicular distance from the ultracataclasite layer of the NBSGF. The combined data for each scale (a-c) is fit by a logarithmic function displayed with the correlation coefficient (R^2). Additionally, the best-fit logarithmic function for the linear subsidiary fault density (LSFD) and linear intragranular fracture density (LIFD) from *Chester et al.* [2005] are displayed.

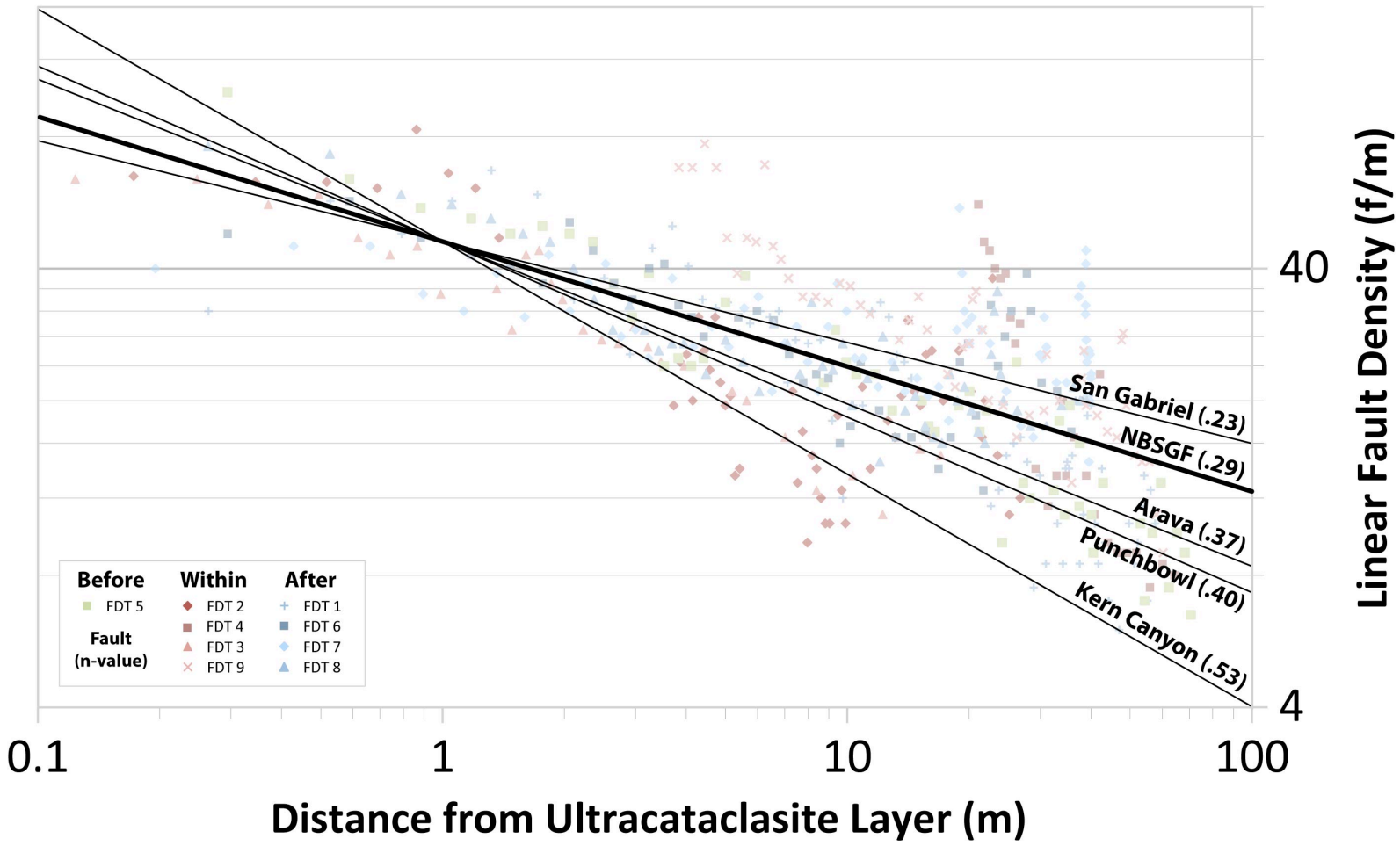

Figure 25. Mature, strike-slip fault's LSFD compared. Displayed in faults per meter (f/m) as a function of perpendicular distance from the ultracataclasite layer of the NBSGF along nine different traverses (Figure 10b). The combined data from each domain is fit by a power law function and compared to other mature, strike slip faults compiled in a previous study [Table 9; *Savage and Brodsky*, 2011].

shallows at very large displacements [Table 9; Figure 25; *Savage and Brodsky*, 2011]. The LSFD trend on the NBSGF appears to support the hypothesis that reactivation of subsidiary faults may be the dominant strain-accommodating process in damage zones associated with the perturbed stress state adjacent to the fault bend [*Faulkner et al.,* 2011; *Savage and Brodsky*, 2011].

The LTFD and LIFD trends shallow significantly to an approximately constant trend, which is significantly more than predicted by the previous studies [Figure 23; *Savage and Brodsky,* 2011]. The trends fit to the microscale data could be the product of enhanced reactivation of preexisting faults and fractures within the damage zone. The constant trends, however, may be the product of low sampling, sampling from only one or two of the mutually perpendicular planes, or unanticipated processes occurring within the fault bend region.

5.2.2. Fabric Orientations and Kinematics Variations in the NBSGF Damage Zone

The mesoscale subsidiary fault data (i.e., fault normals, slip lineations, and b-axes) for the six spatial domains relative to the fault bend (i.e., north and south of the NBSGF, and before, within, and after the bend) show changes in the fabric and kinematics entering and exiting the bend. This is largely compatible with the hypotheses that damage features, specifically shear fractures and subsidiary faults, are reactivated as the damage zone passes geometric irregularities in the fault surface.

The fabric and kinematics of the mesoscale subsidiary faults in the domains east of the bend to the north and south of the fault, and west of the bend to the south of the fault are similar (Figure 26). The fabric along the linear segment of the NBSGF is

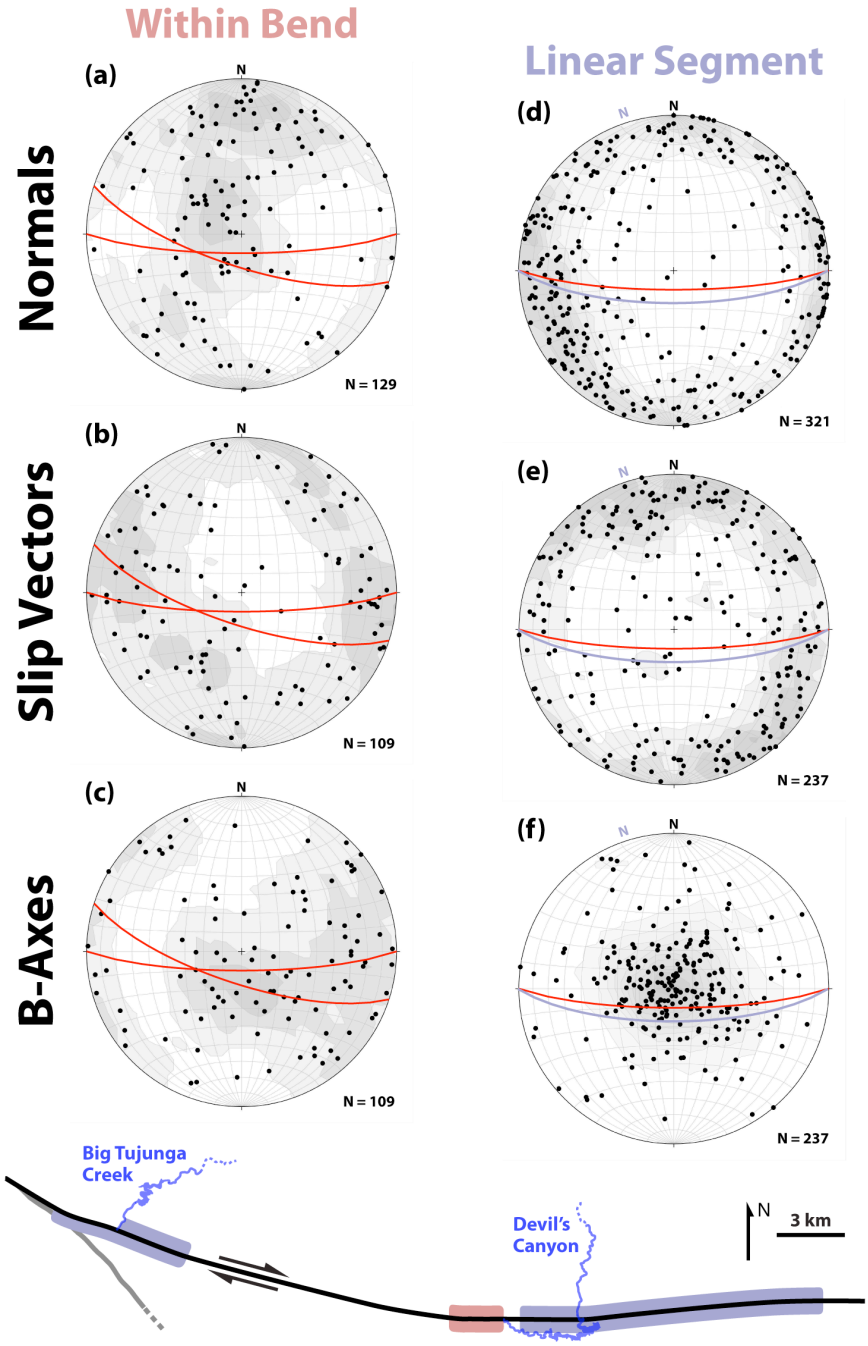

Figure 26. Subsidiary fault orientations and kinematics within bend compared to linear fault segments. Equal-area, lower-hemisphere stereonet projections of poles, slip lineations, and b-axes to subsidiary faults in the NBSGF damage zone, with the average NBSGF orientation (great circles). (a-e) North is at the top, and (d-f) north is at the top for the eastern segment and the data along the western linear segment is rotated 18° counter clockwise to the purple N. A schematic diagram (bottom) shows the relative position of the data located in the domains within (red), and along linear fault segments (purple). Contouring is done using the Kamb method with a contour interval of 2 sigma.

dominated by two subvertical, strike-slip fault sets that form a quasi-conjugate geometry. This geometry defines a maximum principal stress direction that is oriented at a high angle to the NBSGF (Figure 27). The b-axes define a strong point-maximum concentration that are consistent with strike-slip kinematics along the straight segments of the fault. These orientations and kinematics are consistent with field data and cores collected along linear segments of other mature, strike-slip faults with large displacement, such as the Punchbowl and San Andreas Faults, and previous data from the SGF [e.g., *Chester and Logan*, 1987; *Chester et al.,* 1993; *Wilson et al.*, 2003; *Almeida*, 2007].

The domain before the bend to the north and west of Big Tujunga Creek shows a more complex distribution of mesoscale subsidiary fault orientations and kinematics than in other three domains adjacent to long straight segments of the NBSGF (Figure 20). The presence of dominantly dip-slip kinematics with distributed b-axis orientations distinguishes this domain. Furthermore, faults exhibiting dip-slip motion are not observed north of the straight segment before the bend and southeast of Big Tujunga Creek. Dip-slip kinematics in the domain northwest of Big Tujunga Creek likely reflect the fact that many of the fault measurements were made near the junction between the NBSGF and the South Branch of the San Gabriel Fault. The activation of these faults in dip-slip motion may be related to a significant amount of dip-slip motion accommodated on the SBSGF [*F. M. Chester,* Personal communication, 2012]

We interpret that the fabric and kinematics of the subsidiary faults in the damage zones along the straight sections of the fault represent a steady state. East of the NBSGF

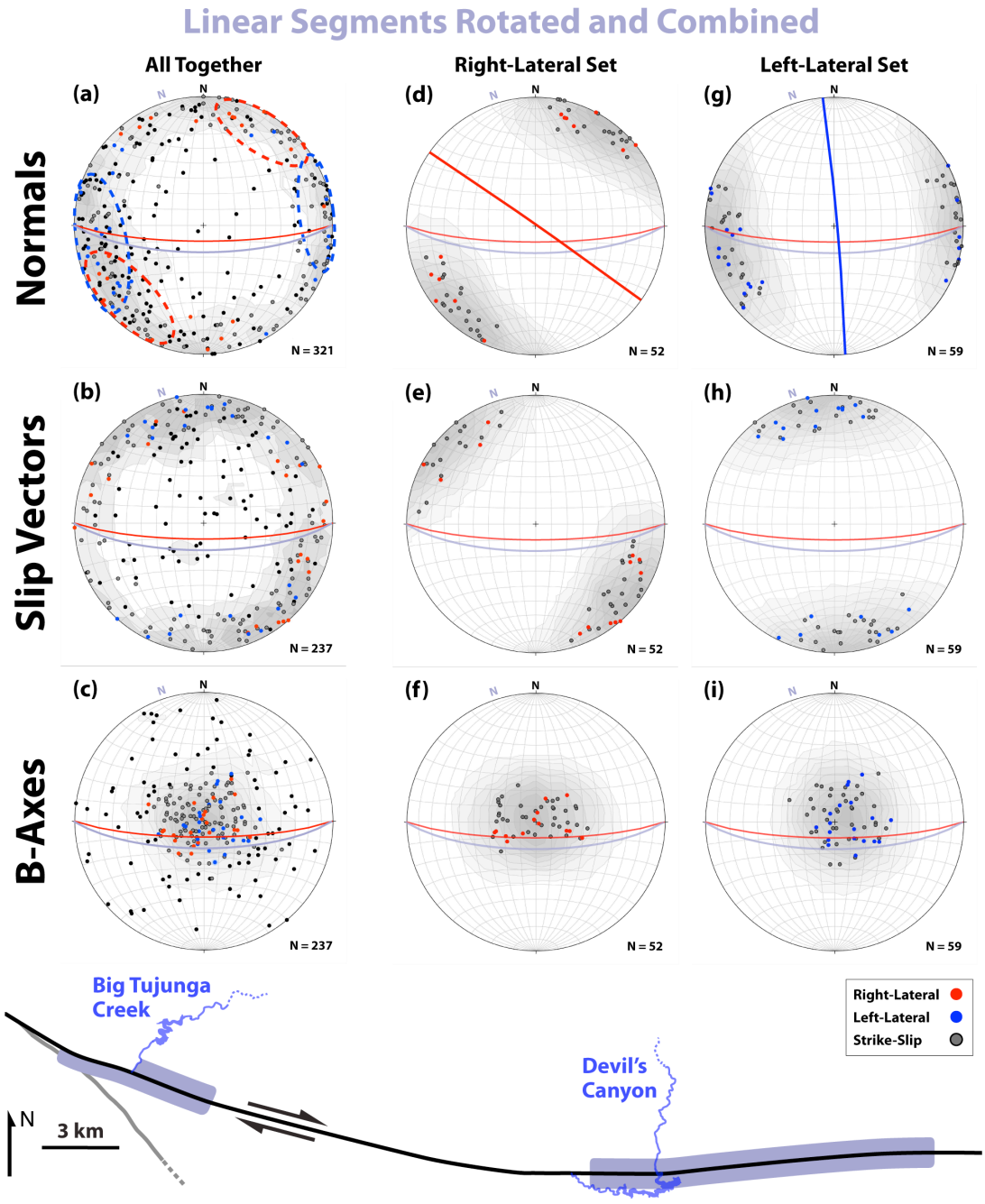

Figure 27. Linear segment subsidiary fault sets orientation and kinematics. Equal-area, lower-hemisphere stereonet projections of poles, slip lineations, and b-axes to subsidiary faults in the NBSGF damage zone, with the average NBSGF orientation (great circles). (a-i) North is at the top for the eastern segment, and the data along the western linear segment is rotated 18° counter clockwise to the purple N. A schematic diagram (bottom) shows the relative position of the data located in the domains along the linear fault segments (purple). Contouring is done using the Kamb method with a contour interval of 2 sigma.

bend, a steady damage state appears to have been achieved before the macroscopic bend (the south side) and after exiting the macroscopic bend (the north side). A similar condition appears to have been established on the west side of the bend and away from the complexity associated with the junction with the South Branch.

There is a significant difference in the mesoscale subsidiary fault fabric and kinematics in the NBSGF damage zone within the fault bend region, as compared to the linear segments of the fault (Figure 26). The domain within the bend exhibits a dominant set of mesoscale subsidiary faults that are subvertical and strike subparallel to the average trend of the NBSGF. This set has slip lineations and b-axes that indicate strike-slip motion (Figure 28). There is also a subhorizontal set of faults present within the bend, which is significantly more prominent north of the fault than to the south. It is important to note that the subhorizontal set is absent in all of the domains along the linear fault segments (Figure 20). Additionally, the subvertical, strike-slip set of mesoscale subsidiary faults that are oriented at high angles to the NBSGF, orientations that dominate the domains adjacent to the linear segments east of the bend and west of the bend to the south, are notably absent from the domains within the bend. These fabrics are consistent with the hypothesis that the subsidiary fault kinematics in the damage zone change upon entering and exiting the bend region.

The microscale transgranular fracture fabric in the damage zone adjacent to the fault bend closely reflects that of the mesoscale subsidiary fault orientations (Figure 29). This is expected, since the majority of the transgranular fractures display some shear, i.e., many are microscopic shear fractures. In order to compare the transgranular fracture

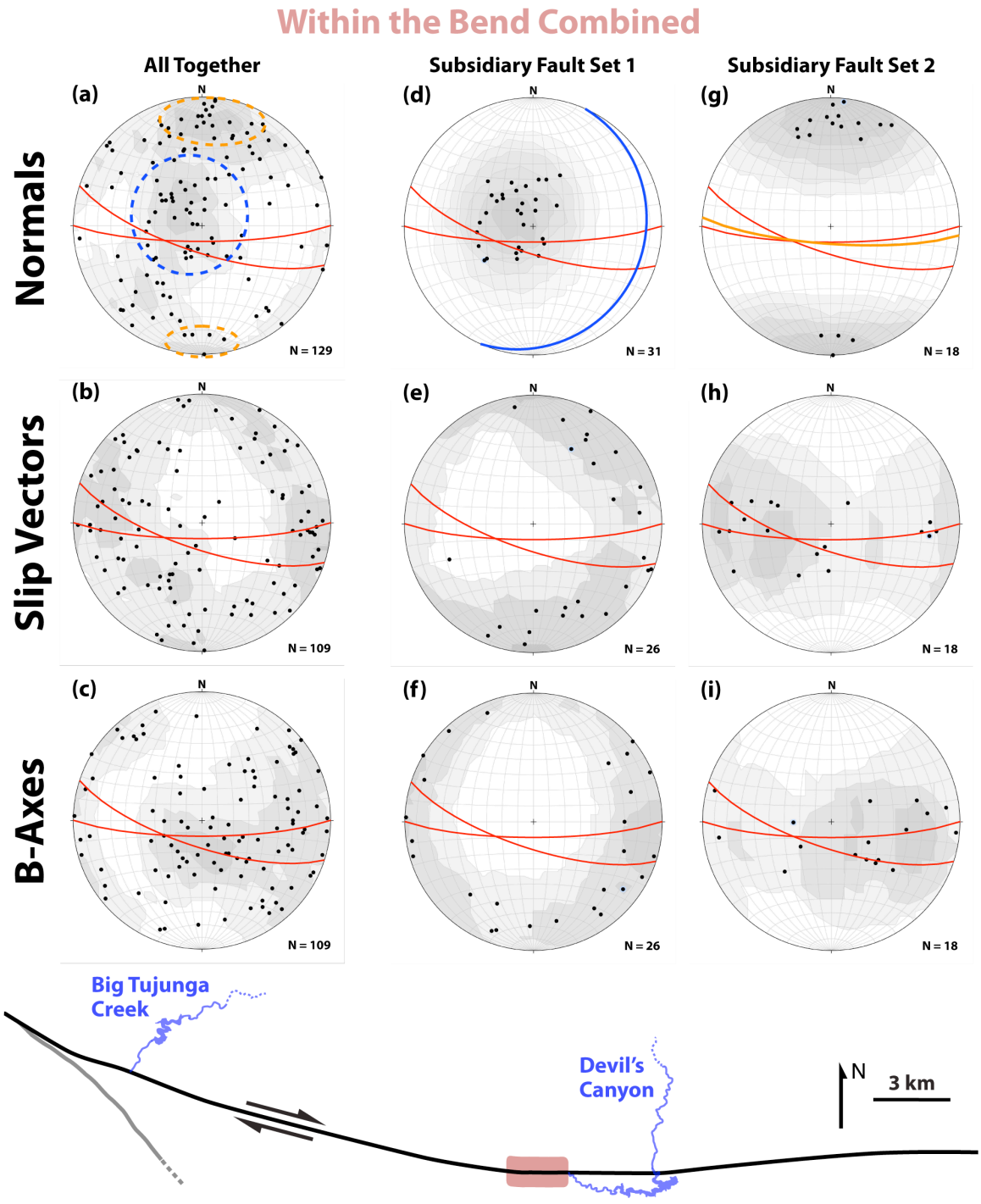

Figure 28. Within bend subsidiary fault sets orientation and kinematics. Equal-area, lower-hemisphere stereonet projections of poles, slip lineations, and b-axes to subsidiary faults in the NBSGF damage zone, with north at the top and the average NBSGF orientation (great circles). A schematic diagram (bottom) shows the relative position of the data located in the domain within the fault bend (red). Contouring is done using the Kamb method with a contour interval of 2 sigma.

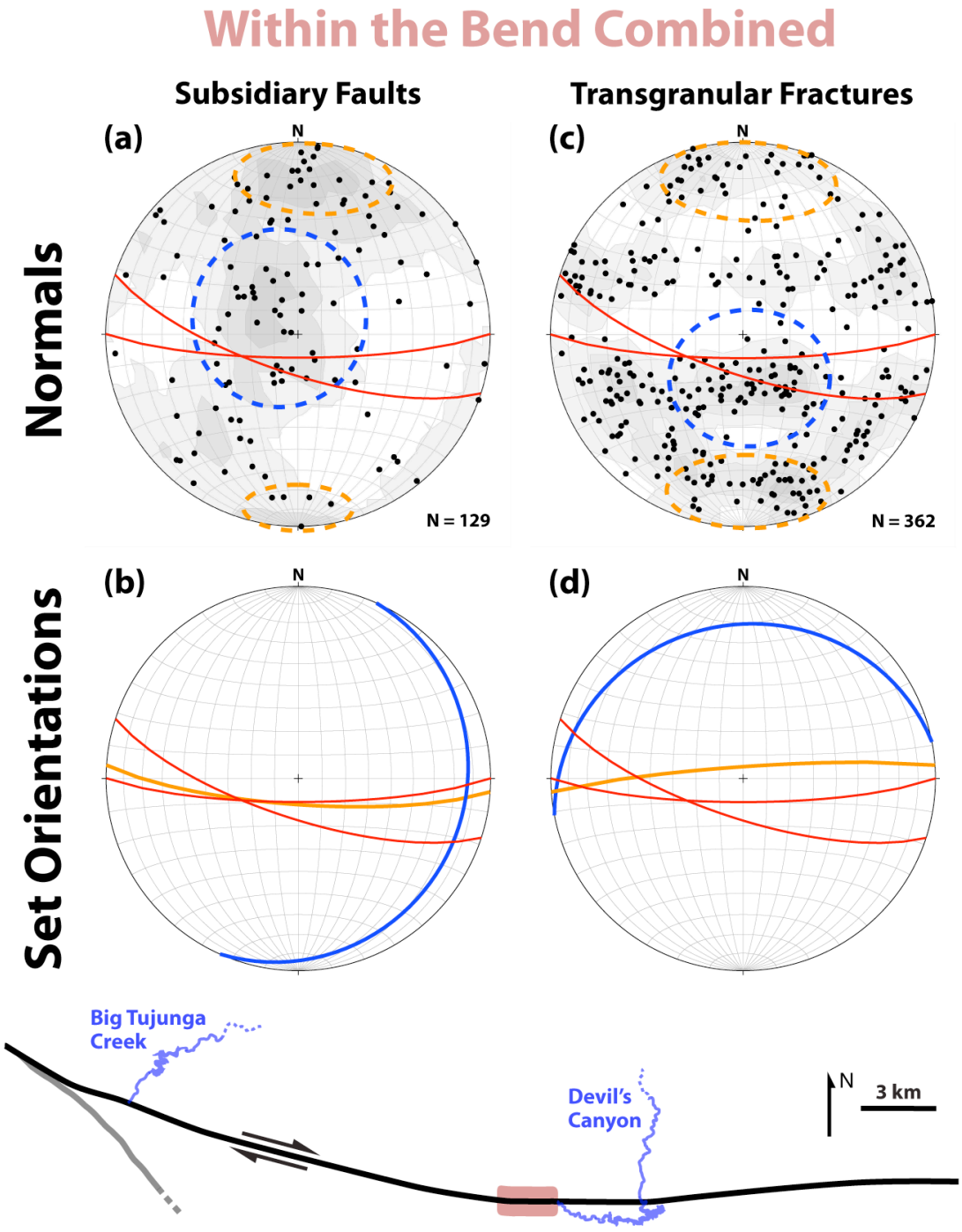

Figure 29. Within bend subsidiary fault and transgranular fracture orientations compared. Equal-area, lower-hemisphere stereonet projections of poles, slip lineations, and b-axes to subsidiary faults in the NBSGF damage zone, with north at the top and the average NBSGF orientation (great circles). (b) A schematic diagram (bottom) shows the relative position of the data located in the domain within the fault bend (red). Contouring is done using the Kamb method with a contour interval of 2 sigma.

fabric with the mesoscale subsidiary fault fabric, only the samples for which transgranular shear fracture fabrics were determined from three mutually perpendicular thin sections are plotted in Figure 21. Subhorizontal and subvertical fractures are present within the given samples, consistent with the unique orientations seen within the bend at the mesoscale (Figure 29).

A comparison between the transgranular fracture and subsidiary fault orientations along the linear fault segments cannot currently be conducted. This is because of low sampling and the lack of three mutually perpendicular thin sections measured in samples from the structural domains adjacent to linear fault segments. Future work completing the transgranular fracture orientation data set is required in order to make a proper comparison to the mesoscale subsidiary fault data in the structural domains outside of the bend region.

5.3. Implications of Fault Bend Effects

The differences between the domains within the bend and those along linear segments suggest that the rock adjacent to the fault bend is in fact subjected to a significantly perturbed stress state. Dynamic earthquake modeling conducted by *Duan and Day* [2008] suggests that the spatial distribution and relative density of deformation associated with a restraining bend is affected greatly by the angle of the bend. Furthermore, there are differences between the north and south sides of the fault within the bend seen in the abundance of features and associated kinematics. The distribution of slip lineations and b-axes within the bend and north of the fault is highly variable compared to all other domains. The concentration of subhorizontal faults is significantly

less within the bend and south of the fault. The differences between the north and south sides of the bend could be associated with the different stress magnitudes and distributions caused by the compressional (concave) versus extensional (convex) sides of the NBSGF bend [*Duan and Day*, 2008].

The absence of new features within the damage zone fabric adjacent to the bend suggests that the density has reached a steady state along the linear segments of the NBSGF. In contrast, as the damage zone translates past the fault bend, a small subset of mesoscale faults and fractures are reactivated as shear fractures that have a range of kinematic signatures. New fault orientations also may have formed in the damage zone as it moves through the fault bend. On the concave side of the fault the damage zone is subjected to compressional stresses due to a reduction in space. Slip along a unique set of faults and fractures accommodates the perturbation associated with the fault bend. Within the fault bend on the convex side of the fault the damage zone is subjected to extensional stresses that produce fewer new damage features relative to the compressional side.

Once the damage zone rock exits the fault bend, the visibility of the subsidiary fault orientation unique to the bend region is reduced almost to zero in both subsidiary faults and transgranular fractures. The reintroduction of the steady-state fault and fracture orientations seen along the linear fault segments occurs in a very short distance after exiting the bend region. This could be due to the reactivation of the more preferentially oriented faults and fractures when reintroduced to the stress state along the linear fault segment. It appears that the reactivation of preexisting features causes those

faults and fractures to become more prominent even with little displacement along the main fault. On the other hand, the linear density remains relatively constant in the structural domains through the fault bend region.

The previous observations exhibit that the reactivation of preexisting features becomes an important process within the bend, and that the creation of new faults and fractures is relatively insignificant. Consequently, during an earthquake, the released elastic strain energy dissipated in the region of a discontinuity, such as a large isolated bend, is more attributed more to frictional heat from reactivation of faults rather than fracture surface energy resulting from the creation of new fractures [*Chester & Chester*, 2006]. Although the amount of reactivation of fractures in the bend relative to outside the bend is difficult to determine from the present data, that kinematics clearly indicate significant reactivation takes place in the bend region. A better estimate could be made from additional modeling of stress and deformation at isolated bends. For such endeavors, the quantification of the variations in the damage zone fabric of the NBSGF provides some constraint on the nature of the deformation that is expected in physics-based dynamic earthquake rupture models of rupture through a large isolated geometric irregularity in a mature fault.

6. SUMMARY AND CONCLUSIONS

Comprehensive analysis of the fault and fracture fabric and kinematics within the North Branch San Gabriel Fault damage zone has shown the following:

1) The orientation distribution of fractures and faults in the damage zone along the linear fault segments of the NBSGF is disturbed in the fault bend region as shown, for example, by the formation of a subhorizontal subsdiary fault set. These new fault orientations almost completely disappear after the fault bend, where the fault fabrics mimic those in the straight segments east of the bend. The new fault and fracture orientations could be accommodating extreme compressional and extensional stresses occurring through the bend, and once exiting the bend.
2) The linear subsidiary fault density, however, remains relatively constant through the bend region. This could mean that the mesoscale subsidiary faults do in fact reach a steady state density, the creation of new mesoscale faults is reduced significantly, and reactivation of subsidiary faults becomes a dominant process. These observations are consistent with our hypothesis that the accumulation of new damage decreases as faults mature, and damage magnitudes saturate at very large displacements.
3) The microscale linear fracture density data (linear transgranular and intragranular fracture densities), for the most part, show similar distributions with distance from the fault, but are different than the mesoscopic density data. This difference

is difficult to explain, and could be the product of low sampling, lack of three-dimensional analysis of key samples, or unanticipated processes occurring through the bend. Additional data is needed to address these issues.

The observations reported indicate that the damage zone of a mature fault reaches an approximate steady-state condition along linear segments of the fault. While passing a large-scale geometric irregularity (i.e., restraining fault bends), the damage zone is subjected to a significantly perturbed stress state. Preexisting fractures in the damage zone are reactivated at restraining fault bends, and the magnitude of reactivation is greater on the compressional (concave) side of the fault. When exiting the fault bend, however, the stress state returns to what it was before entering the bend, and the fabric is reset back to the original steady state. Shear movement along preexisting fracture surfaces to accommodate extension on the outer bend and compression on the inner bend may lead to an increase in the dissipation of energy. If so, the fault bend will act as an energy sink and reduce rupture propagation speeds.

In order to better confirm the present findings, future analysis of the microscale fabrics in the samples not completely analyzed for 3D fabrics should be conducted. Also, additional fieldwork along the NBSGF as well as additional geometric asperities should be pursued.

REFERENCES

Almeida, R. (2007), Mesoscale fracture fabric and paleostress along the San Andreas Fault at SAFOD, M.S. Thesis, Department of Geology and Geophysics, Texas A&M University, College Station, Texas.

Anders, M. H., and D. V. Wiltschko (1994), Microfracturing, paleostress and the growth of faults, *Journal of Structural Geology*, 16(6), 795-815.

Anderson, E. M. (1942), The dynamics of faulting and dyke formation: with Applications to Britain, *Nature*, 149(3789), 651-652.

Anderson, J. L., R. H. Osborne, and D. F. Palmer (1983), Cataclastic rocks of the San Gabriel Fault – An expression of deformation at deeper crustal levels in the San Andreas Fault zone, *Tectonophysics*, 98, 209-251.

Andrews, D. J. (2005), Rupture dynamics with energy loss outside the slip zone, *Journal of Geophysical Research*, 110, B01307, doi:10.1029/2004JB003191.

Bailey, E. H., and R. E. Stevens (1960), Selective staining of k-feldspar and plagioclase on rock slabs and thin sections, *The American Mineralogist*, 45, 1020-1025.

Biegel, R. L., C. G. Sammis, and A. J. Rosakis (2008), An experimental study of the effects of off-fault damage on the velocity of a slip pulse, *Journal of Geophysical Research*, 113, B04302, doi:10.1029/2007JB005234.

Blenkinsop, T. G. (2008), Relationship between faults, extension fractures and veins, and stress, *Journal of Structural Geology*, 30(5), 622-632.

Blythe, A. E., D. W. Burbank, K. A. Farley, and E. J. Fielding (2000), Structural and topographic evolution of the central Transverse Ranges, California, from apatite fission-track, (U–Th)/He and digital elevation model analyses, *Basin Research*, 12, 97-114.

Brace, W. F., and E. G. Bombolakis (1963), A note of brittle crack growth in compression, *Journal of Geophysical Research*, 68(12), 3709-3713.

Chester, F. M., and J. S. Chester (1998), Ultracataclasite structure and friction processes of the Punchbowl Fault, San Andreas system, California, *Tectonophysics*, 295, 199-221.

Chester, F. M., and J. S. Chester (2000), Stress and deformation along wavy frictional faults, *Journal of Geophysical Research*, 105(B10), 23,421-23,430.

Chester, F. M., and J. M. Logan (1986), Implications for mechanical properties of brittle faults from observations of the Punchbowl Fault zone, California, *Pure and Applied Geophysics*, 124(1/2), 79-106.

Chester, F. M., and J. M. Logan (1987), Composite planar fabric of gouge from the Punchbowl Fault, California, *Journal of Structural Geology*, 9(5/6), 621-634.

Chester, F. M., J. S. Chester, D. L. Kirschner, S. E. Schulz, and J. P. Evans (2004), Structure of large-displacement, strike-slip fault zones in the brittle continental crust, in *Rheology and deformation in the lithosphere at continental margins*, edited by Karner, G. D., B. Taylor, N. W. Driscoll, and D. L. Kohlstedt, pp. 223-260, Columbia University Press, New York.

Chester, F. M., J. P. Evans, and R. L. Biegel (1993), Internal structure and weakening mechanisms of the San-Andreas Fault, *Journal of Geophysical Research*, 98(B1), 771-786.

Chester, J. S., F. M. Chester, and A. K. Kronenberg (2005), Fracture surface energy of the Punchbowl Fault, San Andreas system, *Nature*, 437, 133-136.

Chester, J S, Chester, F M, (2006), Energy Dissipation and Damage Generation in Seismic Fault Zones, *Eos Trans. AGU*, 87(52), Fall Meet. Suppl., Abstract T31FF-05.

Chester, J. S., and R. C. Fletcher (1997), Stress distribution and failure in anisotropic rock near a bend on a weak fault, *Journal of Geophysical Research*, 102(B1), 693-708.

Cowie, P. A., and C. H. Scholz (1992), Physical explanation for the displacement-length relationship of faults using a post-yield fracture mechanics model, *Journal of Structural Geology*, 14(10), 1133-1148.

Crowell, J. C. (1982b), The violin breccia, Ridge Basin, southern California, in *Geologic history of Ridge Basin, southern California: Los Angeles, Pacific Section*, edited by Crowell, J.C., and Link, M.H., Society of Economic Paleontologists and Mineralogists, 89-98.

Duan, B., S. M. Day (2008), Inelastic strain distribution and seismic radiation from rupture of a fault kink, *Journal of Geophysical Research*, 113, B12311, doi:1029/2008JB005847.

Dekker, F., H. Balkwill, A. Slater, R. Herner, and W. Kampschuur (1991), Exploring Papua New Guinea with remote sensing, fieldwork, *World Oil*, 221(3), 71-86.

Ehlig, P.L. (1973), History, seismicity, and engineering geology of the San Gabriel Fault, in *Geology, seismicity, and environmental impact: Association of Engineering Geologists special publication*, edited by Moran, D. E., Slosson, J. E., Stone, R. O., and Yelverton, C. A., pp. 247-251, University of Michigan Press, Michigan.

Ehlig, P. L. (1981), Origin and tectonic history of the basement terrane of the San Gabriel Mountains, central Traverse Ranges, in *The geotectonic development of California*, vol. 1, edited by W. G. Ernst, pp. 253-283, Prentice Hall, New Jersey.

Evans, J. P., and F. M. Chester (1995), Fluid-rock interaction in the faults of the San Andreas system: Inferences from San Gabriel Fault rock geochemistry and microstructures, *Journal of Geophysical Research*, 100(B7), 13,007-13,020.

Faulkner, D. R., C. A. L. Jackson, R. J. Lunn, R. W. Schlische, Z. K. Shipton, and C. A. J. Wibberley, M. O. Withjack (2010), A review of recent developments concerning the structure, mechanics and fluid flow properties of fault zones, *Journal of Structural Geology*, 32, 1557-1575.

Faulkner, D. R., T. M. Mitchell, E. Jensen, and J. Cembrano (2011), Scaling of fault damage zones with displacement and the implications for fault growth processes, *Journal of Geophysical Research*, 116, B05403, doi:10.1029/2010JB007788.

Flinn, D. (1977), Transcurrent faults and associated cataclasis in Shetland, *Journal of the Geological Society London*, 133(3), 231-248.

Friedman, M. (1969), Structural analysis of fractures in cores from the Saticoy Field, Ventura Co., California, *American Society of Petroleum Geology Bulletin*, 53, 367-389.

Gabriel, A., and E. P. Cox (1929), A staining method for the quantitative determination of certain rock minerals, *The American Mineralogist*, 14, 290-292.

Harris, R., and M. Cooper (2002), Structural analysis in eastern Yemen using remote sensing data, *World Oil*, 23(11), 52-57.

Harris, R. A., and S. M. Day (1999), Dynamic 3D simulations of earthquakes on en echelon faults, *Geophysical Research Letters*, 26(14), 2089-2092.

Janssen, C., R. L. Romer, A. Hoffman-Rothe, D. Kesten, and H. Al-Zubi (2004), The Dead Sea Transform: Evidence for a strong fault?, *Journal of Geology*, 112, 561-575, doi:10.1086/422666.

Kanamori, H. (1994), Mechanics of earthquakes, *Annual Review of Earth and Planetary Sciences*, 22, 207-237.

Kanamori, H., and T. H. Heaton (2000), Microscopic and macroscopic physics of earthquakes, in *GeoComplexity and the physics of earthquakes*, edited by Rundle, J. B., D. L. Turcotte, and W. Klein, pp. 127-141, Geophysical Monograph 20, American Geophysical Union, Washington D.C.

King, G., and J. Nabelek (1985), Role of fault bends in the initiation and termination of earthquake rupture, *Science*, 228(4702), 984-987.

Kulander, B. R., C. C. Barton, and S. L. Dean (1979), The application of fractography to core and outcrop fracture investigation, *Morgantown Energy Technology Center*, report prepared for U.S. Department of Energy METC/SP, 79(3), 1-174.

Laubach, S. E. (1988), Subsurface fractures and their relationship to stress history in East Texas basin sandstone, *Tectonophysics*, 156, 37-49.

Le Bas, M. J., and A. L. Streckeisen (1991), The IUGS systematics of igneous rocks, *Journal of the Geological Society, London*, 148, 825-833.

Lockner, D. A., J. D. Byerlee, V. Kuksenko, A. Ponomarev, and A. Sidorin (1991), Quasi-static fault growth and shear fracture energy in granite, *Nature*, 350(6313), 39-42.

Lockner, D. A., D. E. Moore, and Ze'ev Reches (1992), Microcrack interaction leading to shear fracture, in *Fault mechanics and transport properties of rocks*, vol. 51, edited by B. Evens, and T-f. Wong, pp. 33-67, Academic Press, London.

Luo, W., and T. Stepinski (2008), Identification of geologic contrasts from landscape dissection pattern: An application to the Cascade Range, Oregon, USA, *Geomorphology*, 99, 90-98.

Mitchell, T. M., and D. R. Faulkner (2009), The nature and origin of off-fault damage surrounding strike-slip fault zones with a wide range of displacements: A field study from the Atacama Fault system, northern Chile, *Journal of Structural Geology*, 31(8), 802-816.

Morton, D. M., and J. C. Matti (1987), The Cucamonga Fault zone, geologic setting and Quaternary history, *United States Geologic Survey Professional Paper*, 1339.

Neal, L. A. (2002), Internal structure of the Kern Canyon Fault, California: A deeply exhumed strike-slip fault, M.S. Thesis, Department of Geology and Geophysics, Texas A&M University, College Station, Texas.

Oakeshott, G. B. (1971), Geology of the epicentral area, *California Division of Mines and Geology*, 196, 19-30.

Powell, R. E. (1993), Balanced palinspastic reconstruction of prelate Cenozoic paleogeology, southern California: Geologic and kinematic constraints on evolution of the San Andreas fault system, in *The San Andreas Fault system: Displacement, palinspastic reconstruction, and geologic evolutions*, edited by R. E. Powell, R. J. Weldon, II, and J. C. Matti, pp. 1-106, Geological Society of America Memoir 178, Boulder, Colorado.

Power, W. L., and T. E. Tullis (1991), Euclidean and fractal models for the description of rock surface roughness, *Journal of Geophysical Research*, 96(B1), 415-424.

Rice, J. R., C. G. Sammis, and R. Parsons (2005), Off-fault secondary failure induced by a dynamic slip pulse, *Bulletin of the Seismological Society of America*, 95(1), 109-134.

Sagy, A., and E. E. Brodsky (2009), Geometric and rheological asperities in an exposed fault zone, *Journal of Geophysical Research*, 114, B02301, doi:10.1029/2008JB005701.

Savage, H. M., and E. E. Brodsky (2011), Collateral damage: Evolution with displacement of fracture distribution and secondary fault strands in fault damage zones, *Journal of Geophysical Research*, 116, B03405, doi:10.1029/2010JB007665.

Segall, P., and D. D. Pollard (1980), Mechanics of discontinuous faults, *Journal of Geophysical Research*, 85(B8), 4337-4350.

Segall, P., and D. D. Pollard (1983), Joint formation in granitic rock of the Sierra Nevada, *Geological Society of America Bulletin*, 94, 563-575.

Scholz, C. H., N. H. Dawers, J.-Z. Yu, M. H. Anders, and P. A. Cowie (1993), Fault growth and fault scaling laws: Preliminary results, *Journal of Geophysical Research*, 98(B12), 21,951-21,961.

Sammis, C., G. King, and R. Biegel (1987), The kinematics of gouge deformation, *Pure and Applied Geophysics*, 125, 777-812.

Sammis, C. G., A. J. Rosakis, and H. S. Bhat (2009), Effects of off-fault damage on earthquake rupture propagation: Experimental studies, *Pure and Applied Geophysics*, 166, 1629-1648.

Saucier, F., E. Humphreys, and R. Weldon II (1992), Stress near geometrically complex strike-slip faults: Application to the San Andreas Fault at Cajon Pass, southern California, *Journal of Geophysical Research*, 97(B4), 5081-5094.

Takagi, H., K. Takahashi, K. Shimada, K. Tsutsui, R. Miura, N. Kato, and S. Takizawa (2012), Integrated estimates of the thickness of the fault damage zone in granitic terrain based on penetrative mesocracks and XRD analyses on quartz, *Journal of Structural Geology*, 35, 64-77.

Templeton, E. L., and J. R. Rice (2008), Off-fault plasticity and earthquake rupture dynamics: 1. Dry materials or neglect of fluid pressure changes, *Journal of Geophysical Research*, 113, B09306, doi:10.1029/2007JB005529.

Venkataraman, A., and H. Kanamori (2004), Observational constraints on the fracture energy of subduction zone earthquakes, *Journal of Geophysical Research*, 109, B05302, doi:10.1029/2003JB002549.

Vermilye, J. M., and C. H. Scholz (1998), The process zone: A microstructural view of the fault growth, *Journal of Geophysical Research*, 103(B6), 12,223-12,237.

Wallace, R. E., and H. T. Morris (1986), Characteristics of fault and shear zones in deep mines, *Pure and Applied Geophysics*, 124(1/2), 107-125.

Wechsler, N., T. K. Rockwell, and Y. Ben-Zion (2009), Application of high resolution DEM data to detect rock damage from geomorphic signals along the central San Jacinto Fault, *Geomorphology*, 113(1-2), 82-96.

Wesnousky, S. G. (2006), Predict the endpoint of earthquake ruptures, *Nature*, 444, 358-360.

Wesnousky, S. G. (1988), Seismological and structural evolution of strike-slip faults, *Nature*, 335, 340-343.

Wilson, J. E., J. S. Chester, and F. M. Chester (2003), Microfracture analysis of fault growth and wear processes, Punchbowl Fault, San Andreas system, California, *Journal of Structural Geology*, 25, 1855-1873.

Wilson, J. E. (1999), Microfracture fabric of the Punchbowl Fault zone, San Andreas system, California, M.S. Thesis, Department of Geology and Geophysics, Texas A&M University, College Station, Texas.